



HAL
open science

The Role of Tidal Mixing in Shaping Early Eocene Deep Ocean Circulation and Oxygenation

Jean-Baptiste Ladant, Jeanne Millot-Weil, Casimir de Lavergne, J. A. Mattias Green, Sébastien Nguyen, Yannick Donnadieu

► **To cite this version:**

Jean-Baptiste Ladant, Jeanne Millot-Weil, Casimir de Lavergne, J. A. Mattias Green, Sébastien Nguyen, et al. The Role of Tidal Mixing in Shaping Early Eocene Deep Ocean Circulation and Oxygenation. *Paleoceanography and Paleoclimatology*, 2024, 39 (7), pp.e2023PA004822. 10.1029/2023pa004822 . hal-04648189

HAL Id: hal-04648189

<https://hal.science/hal-04648189v1>

Submitted on 15 Jul 2024

HAL is a multi-disciplinary open access archive for the deposit and dissemination of scientific research documents, whether they are published or not. The documents may come from teaching and research institutions in France or abroad, or from public or private research centers.

L'archive ouverte pluridisciplinaire **HAL**, est destinée au dépôt et à la diffusion de documents scientifiques de niveau recherche, publiés ou non, émanant des établissements d'enseignement et de recherche français ou étrangers, des laboratoires publics ou privés.




Paleoceanography and Paleoclimatology



RESEARCH ARTICLE

10.1029/2023PA004822

The Role of Tidal Mixing in Shaping Early Eocene Deep Ocean Circulation and Oxygenation

Jean-Baptiste Ladant¹ , Jeanne Millot-Weil^{1,2}, Casimir de Lavergne³, J. A. Mattias Green⁴ , Sébastien Nguyen¹, and Yannick Donnadiou⁵ 

¹Laboratoire des Sciences du Climat et de l'Environnement, LSCE/IPSL, CEA-CNRS-UVSQ, Université Paris-Saclay, Gif-sur-Yvette, France, ²Now at School of Geographical Sciences, University of Bristol, Bristol, UK, ³LOCEAN Laboratory, Sorbonne Université/IRD/CNRS/MNHN, Paris, France, ⁴School of Ocean Sciences, Bangor University, Menai Bridge, UK, ⁵Aix Marseille Université, CNRS, IRD, INRA, Coll France, CEREGE, Aix-en-Provence, France

Key Points:

- Inclusion of realistic near-field tidal mixing substantially modifies global deep ocean circulation in the Early Eocene
- These tidally driven changes yield significantly different biogeochemical properties of water masses, in particular in the Atlantic
- The simulation that includes tidal mixing compares more favorably to inferences from the O₂ proxy record

Supporting Information:

Supporting Information may be found in the online version of this article.

Correspondence to:

J.-B. Ladant,
jean-baptiste.ladant@lsce.ipsl.fr

Citation:

Ladant, J.-B., Millot-Weil, J., de Lavergne, C., Green, J. A. M., Nguyen, S., & Donnadiou, Y. (2024). The role of tidal mixing in shaping Early Eocene deep ocean circulation and oxygenation. *Paleoceanography and Paleoclimatology*, 39, e2023PA004822. <https://doi.org/10.1029/2023PA004822>

Received 1 DEC 2023
Accepted 26 JUN 2024

Author Contributions:

Conceptualization: Jean-Baptiste Ladant, Casimir de Lavergne, J. A. Mattias Green, Yannick Donnadiou

Formal analysis: Jean-Baptiste Ladant, Jeanne Millot-Weil, Casimir de Lavergne

Funding acquisition: Yannick Donnadiou

Investigation: Jean-Baptiste Ladant, Jeanne Millot-Weil

Methodology: Jean-Baptiste Ladant, Casimir de Lavergne

Project administration: Jean-Baptiste Ladant

Resources: Jean-Baptiste Ladant

Software: Jean-Baptiste Ladant, Jeanne Millot-Weil, Casimir de Lavergne, Sébastien Nguyen

© 2024. The Author(s).

This is an open access article under the terms of the [Creative Commons Attribution License](https://creativecommons.org/licenses/by/4.0/), which permits use, distribution and reproduction in any medium, provided the original work is properly cited.

Abstract Diapycnal mixing in the ocean interior is largely fueled by internal tides. Mixing schemes that represent the breaking of internal tides are now routinely included in ocean and earth system models applied to the modern and future. However, this is more rarely the case in climate simulations of deep-time intervals of the Earth, for which estimates of the energy dissipated by the tides are not always available. Here, we present and analyze two IPSL-CM5A2 earth system model simulations of the Early Eocene made under the framework of DeepMIP. One simulation includes mixing by locally dissipating internal tides, while the other does not. We show how the inclusion of tidal mixing alters the shape of the deep ocean circulation, and thereby of large-scale biogeochemical patterns, in particular oxygen distributions. In our simulations, the absence of tidal mixing leads to a relatively stagnant and poorly ventilated deep ocean in the North Atlantic, which promotes the development of a basin-scale pool of oxygen-deficient waters, at the limit of complete anoxia. The absence of large-scale anoxic records in the deep ocean after the Cretaceous anoxic events suggests that such an ocean state most likely did not occur at any time across the Paleogene. This highlights how crucial it is for climate models applied to the deep-time to integrate the spatial variability of tidally driven mixing as well as the potential of using biogeochemical models to exclude aberrant dynamical model states.

1. Introduction

Tides are the main supplier of diapycnal mixing in the ocean's interior, beneath the surface boundary layer (e.g., de Lavergne et al., 2020; Egbert & Ray, 2000; Vic et al., 2019). Barotropic tidal currents flowing over sloping bottom topography generate internal waves at tidal frequencies, called internal tides (Garrett & Kunze, 2007). The propagation, non-linear interaction, and ultimate breaking of internal tides into three-dimensional turbulence constitutes the primary contribution to diapycnal mixing (i.e., mixing across isopycnals) and thus to water mass transformation in the deep ocean (de Lavergne et al., 2022; Melet et al., 2022). There are multiple pathways and processes leading to the dissipation of internal tide energy. Small-scale internal tides tend to dissipate close to their generation site, whereas large-scale internal tides dissipate more remotely, sometimes thousands of kilometers away from the generation site (Whalen et al., 2020).

The modern global overturning circulation is usually schematized as a two-loop system, consisting of an adiabatic upper cell fed by North Atlantic Deep Water (NADW) formation in the subpolar North Atlantic, overlying a largely diabatic lower cell fed by Antarctic Bottom Water (AABW) formation in the polar Southern Ocean (Marshall & Speer, 2012; Melet et al., 2022; Talley, 2013). Diapycnal mixing plays an important role in shaping this two-cell overturning circulation (Cimoli et al., 2023); in particular the tidally driven, bottom-intensified, part of the mixing is instrumental in reducing the density of northward-flowing AABW and in mixing AABW with NADW (de Lavergne et al., 2022; Melet et al., 2022). It is the specific geometry of the modern Southern Ocean, with its continent-free latitudinal band down to a depth of ~2,000 m at the Drake Passage, that favors the adiabatic upwelling of deep waters (NADW and Pacific/Indian Deep Waters) (Toggweiler & Samuels, 1995, 1998) as the residual of surface wind-driven and eddy-driven circulations in the Southern Ocean (Marshall & Speer, 2012). This prompts the possibility that, in periods of the deep-time past of the Earth when the Drake and/or Tasman gateways were closed or shallow, diapycnal (diabatic) mixing may have played a greater role in setting the mode and intensity of the global overturning circulation (Green & Huber, 2013).

Supervision: Jean-Baptiste Ladant, Yannick Donnadiou
Validation: Jean-Baptiste Ladant
Visualization: Jean-Baptiste Ladant
Writing – original draft: Jean-Baptiste Ladant
Writing – review & editing: Jean-Baptiste Ladant, Jeanne Millot-Weil, Casimir de Lavergne, J. A. Mattias Green, Sébastien Nguyen, Yannick Donnadiou

Since the seminal work of Munk (1966), great efforts have been made to understand what controls diapycnal mixing in the ocean interior (e.g., MacKinnon et al., 2017; Munk & Wunsch, 1998; St. Laurent & Garrett, 2002) and to refine the parameterizations of vertical diffusivity in ocean general circulation models (GCM) (e.g., Bryan & Lewis, 1979; de Lavergne et al., 2020; Gargett, 1984; Jayne, 2009; Melet et al., 2016; Saenko & Merryfield, 2005; Schmittner & Egbert, 2014; Simmons et al., 2004; Song et al., 2023). Recent work has comprehensively reviewed what is currently known about the role of ocean mixing in the climate system (de Lavergne et al., 2022; Melet et al., 2022; Whalen et al., 2020) and, in particular, the contribution of different internal wave processes (e.g., near-field and far-field internal tide dissipation, lee wave dissipation and wind-induced near-inertial wave energy dissipation) to the total mixing. The parameterization of all of these processes into global ocean models is a currently active area of research (MacKinnon et al., 2017) and, in climate models applied to the deep-time past of the Earth, such processes are generally ignored. Instead, mixing in the ocean interior is parameterized either by a constant background diffusivity coefficient or by simple schemes such as a horizontally uniform but depth varying diffusivity profile (Bryan & Lewis, 1979, hereafter BL).

In recent years though, some models applied to paleoclimate studies have started to include the contribution of local (near-field) internal tide dissipation (e.g., Hutchinson et al., 2018; Schmittner et al., 2015; Wilmes et al., 2021), following the bottom-intensified mixing parameterization of Simmons et al. (2004, hereafter S04). Wilmes et al. (2021) notably show that using appropriate Last Glacial Maximum tidal dissipation, instead of modern dissipation with otherwise glacial forcings, invigorates the circulation in the ocean interior and increases the fit with carbon isotope measurements. Hutchinson et al. (2018) compare the S04 scheme with the previously implemented BL scheme in Late Eocene GFDL CM2.1 earth system model simulations and essentially find very little differences in terms of ocean circulation structure and intensity and of water mass age. This echoes the same exercise performed by Jayne (2009) using modern simulations carried out with the NCAR POP 1.4.3 ocean model. Jayne (2009) investigates how the modern ocean circulation is affected by different abyssal mixing parameterizations, in particular a flat mixing case with a constant background diffusivity, a standard BL parameterization and the explicit S04 scheme for locally dissipating internal tides. At low-resolution (3°), the different simulations of Jayne (2009) exhibit similar intensities of the Atlantic Meridional Overturning Circulation (MOC) and abyssal MOC, with maximum relative changes of ~2.5 Sv, and little differences in Ocean Heat Transport (OHT). At higher resolution (1°), the change from BL to S04 still barely affects the simulated OHT and upper ocean circulation (because of similar vertical diffusivity values there) but significantly increases the intensity of the deep circulation from 17 to 22.3 Sv (Jayne, 2009).

More recently, Zhang et al. (2022) have explored the variability in ocean circulation in models participating to the DeepMIP project on the Early Eocene (Lunt et al., 2017). These models use various parameterizations of vertical diffusivity, most of them variations around the standard BL profile (Zhang et al., 2022), but two of them explicitly include the S04 scheme (IPSL-CM5A2 and GFDL). The models were forced by a set of Early Eocene forcings, identical across the models but for the details of their implementation. The authors report large inter-model differences in simulated ocean circulation structure and intensity (Zhang et al., 2022, their Figure 2): IPSL-CM5A2, MIROC and CESM exhibit intense abyssal overturning (~16 Sv at 3,000 m depth); GFDL, COSMOS and HadCM3B show overturning rates about half as strong at the same depth (~8–10 Sv at 3,000 m depth); and NorESM shows almost no overturning (<4 Sv below 1,500 m), although the deep ocean may be far from equilibrium in this experiment. Interestingly, the two models including explicit local tidal dissipation show contrasting ocean circulations. IPSL-CM5A2 simulates a vigorous circulation throughout the water column, which is fed by Southern Ocean waters and extends to the northern high latitudes, whereas GFDL exhibits a weaker circulation, which is fed by North Pacific waters and barely penetrates the abyssal Southern Hemisphere (Figure 2 of Zhang et al. (2022)). It is possible that the difference in simulated circulation relates to the different deep ocean ventilation areas in IPSL-CM5A2 and GFDL, which can affect the amount of deep water formed and the deep ocean stratification, or to the different energy input to tidal dissipation in the S04 scheme (computed following Equation 2 of S04 in GFDL whereas using the estimates from Green and Huber (2013) in IPSL-CM5A2). Though reasons for this >6 Sv difference in the intensity of abyssal overturning are not yet elucidated and require further investigation, it nonetheless suggests that deep ocean tidal mixing exerts a primary control on the Early Eocene deep ocean circulation.

Here, we therefore focus more closely on the mechanisms by which the inclusion of near-field bottom-intensified tidal mixing (using the S04 parameterization) impact the ocean circulation and biogeochemistry in the Early

Eocene. We demonstrate that failing to include abyssal turbulent mixing leads to relatively stagnant deep seas with large areas of anoxia, in disagreement with proxy data from the Equatorial and North Atlantic.

2. Model and Simulations

2.1. IPSL-CM5A2 Earth System Model

The simulations presented in this work are performed with the IPSL-CM5A2 Earth System Model (Sepulchre et al., 2020), itself composed of LMDZ for the atmosphere (Hourdin et al., 2013), ORCHIDEE for the land surface and vegetation (Krinner et al., 2005), and NEMO version 3.6 for the ocean (Madec et al., 2017). NEMOv3.6 consists of the OPA dynamic ocean model, the LIM2 sea-ice model (Fichefet & Maqueda, 1997) and the PISCES-v2 marine biogeochemistry model (Aumont et al., 2015). OASIS (Valcke, 2013) is used to couple the models, and XIOS (Meurdesoif et al., 2016) handles input/output processing. LMDZ and ORCHIDEE share the same horizontal resolution of $3.75^\circ \times 1.875^\circ$ (longitude \times latitude) and LMDZ is discretized into 39 uneven levels in the vertical. NEMO has a nominal horizontal resolution of 2° , enhanced to 0.5° at the equator, and 31 vertical levels whose thickness varies from 10 m at the surface to 500 m at the bottom. NEMO uses a tripolar grid to overcome the North Pole singularity (Madec & Imbard, 1996). Previous deep-time paleoclimate modeling with the IPSL-CM5A2 model (e.g., Laugié et al., 2021), including the IPSL-CM5A2 simulations carried out as part of the DeepMIP project (Zhang et al., 2020, 2022), used an oceanic domain extending down to 78°S . Here the numerical ocean grid has been regenerated and extended southward in latitude down to 85°S in order to better represent possible marine incursions at latitudes poleward of 78°S in intervals of the last 100 Ma. We note that this represents a negligible issue in the standard DeepMIP paleogeography based on a hotspot reference frame that we use here; however, this would not be the case in Early Eocene paleogeographies constructed with a paleomagnetic reference frame (Lunt et al., 2017).

2.2. Mixing in the Ocean Model

In this version of NEMO, vertical mixing in the water column is implemented as a Turbulent Kinetic Energy (TKE) closure model (Blanke & Delecluse, 1993; Gaspar et al., 1990). This closure is complemented with a parameterization for convection, consisting of enhanced vertical diffusion where stratification is unstable (Lazar et al., 1999), a parameterization for double diffusive mixing (Merryfield et al., 1999), and a tidal mixing parameterization following S04. The vertical eddy diffusivity coefficient K_v is thus expressed as:

$$K_v = \max(K_0, K_{\text{TKE}}) + K_{\text{ddm}} + K_{\text{Tides}} \text{ for } N^2 > 0 \text{ (stable stratification)}$$

$$K_v = K_{\text{EVD}} \text{ otherwise}$$

with N the Brunt-Väisälä frequency, K_0 a background diffusivity effectively setting the minimum vertical diffusivity, K_{TKE} the diffusivity computed from the TKE scheme, K_{ddm} the diffusivity attributed to double diffusion, K_{Tides} the tidal diffusivity and K_{EVD} a prescribed constant convective diffusivity. Strictly speaking, the tidal and double diffusion schemes contribute to K_v even in regions of unstable stratification but the very large diffusivity value parameterizing convective processes renders these contributions negligible. Here, K_0 is set to $1.2 \times 10^{-5} \text{ m}^2 \text{ s}^{-1}$, $K_{\text{EVD}} = 100 \text{ m}^2 \text{ s}^{-1}$ and K_{Tides} has the form:

$$K_{\text{Tides}}(x, y, z) = \frac{q\Gamma E(x, y) F(z)}{\rho N^2(x, y, z)} \quad (1)$$

where q is the tidal dissipation efficiency, Γ is the mixing efficiency, $E(x, y)$ is the power lost by the barotropic tide (gained by internal tides) per unit area from Green and Huber (2013), ρ is the water density, N is the buoyancy frequency along the seafloor and $F(z)$ is a vertical structure function that decays exponentially with height above bottom:

$$F(z) = \frac{e^{-\frac{H+z}{h_0}}}{h_0 \left(1 - e^{-\frac{H}{h_0}}\right)} \quad (2)$$

with H the total depth of the water column, h_0 the vertical decay scale for turbulence and z the model depth.

We use the standard model values of $q = \frac{1}{3}$, $\Gamma = 0.2$ and $h_0 = 500$ m (Madec et al., 2017), which are identical to those originally chosen by S04.

2.3. PISCES Marine Biogeochemistry Model

The PISCES model (Pelagic Interactions Scheme for Carbon and Ecosystem Studies, Aumont et al., 2015) simulates the lower trophic levels of marine ecosystems (nanophytoplankton, diatoms, microzooplankton, and mesozooplankton), carbonate chemistry and the biogeochemical cycles of carbon, oxygen, and the main nutrients (phosphorus, nitrogen, iron, and silica). Dissolved oxygen is produced in the ocean by phytoplankton net primary production and consumed by zooplankton heterotrophic respiration, oxic remineralization of organic matter and nitrification. At the air-sea interface, dissolved oxygen is exchanged using the parameterization of Wanninkhof (1992). The atmospheric concentration of dioxygen is set to a fixed ratio of 0.21.

In the water column, PISCES explicitly represents two pools of organic matter particles that differ in their average size (i.e., large and small particles) and respective sinking speed, as well as a pool of semi-labile dissolved organic matter. The particle pools are degraded into the dissolved one as a function of temperature and oxygen concentrations. Dissolved organic matter undergoes oxic remineralization or denitrification depending on local oxygen levels. The remineralization and denitrification rates are function of temperature, oxygen and nitrate concentrations, and of the bacterial activity and biomass (Aumont et al., 2015). When reaching the ocean floor in the form of particles, organic matter is permanently buried or degraded by sedimentary denitrification or oxic remineralization. The proportion of buried carbon is dependent on the organic carbon flux at the bottom and is computed according to Dunne et al. (2007). The fraction of sedimentary denitrification versus oxic remineralization is computed using the meta-model of Middelburg et al. (1996). Degraded organic carbon is then released into the ocean bottom level in the form of DIC. Ocean bottom concentrations of dissolved oxygen and nitrate are also consumed to account for sedimentary oxic remineralization and denitrification, respectively (Aumont et al., 2015). In the absence of an explicit sediment module, the global inventories in phosphate, nitrate, silicate and alkalinity are restored to modern values so that the global mean ocean concentrations in these elements do not drift away from modern mean concentrations (Aumont et al., 2015). We also use an additional inert artificial tracer representing the age of water masses. This age tracer value is restored to 0 in the top 10 m of the model ocean and increases at a rate of 1 year per year deeper than 10 m (Bopp et al., 2017).

2.4. Experimental Design

We present two numerical simulations of the Early Eocene based on the DeepMIP protocol (Lunt et al., 2017). The boundary and initial conditions are essentially those of the 840 ppmv simulations of Zhang et al. (2020), that is, we use the paleogeography of Herold et al. (2014) with a prescribed atmospheric CO_2 concentration of 840 ppmv. The orbital parameters of the Earth are those of present-day and other greenhouse gas concentrations are set to their preindustrial values. The simulations are therefore representative of a pre-Paleocene-Eocene Thermal Maximum interval, following the terminology of Lunt et al. (2017). The simulations are initialized with ocean temperature and salinity distributions as in Zhang et al. (2020) and only differ by the absence (“EE-noM2”) or presence (“EE-std”) of the contribution of near-field internal tide energy dissipation (K_{Tides}) to the vertical diffusivity coefficient. In the following, we will refer to the absence or presence of tidal mixing, though this is somewhat a misnomer because the contribution of background diffusivity (i.e., K_0) to vertical diffusivity is included in the two simulations. As described in S04, this background diffusivity may account for the far-field dissipation of large-scale internal tides as well as other sources of mixing that are not explicitly modeled, such as lee waves or wind-induced radiating near-inertial waves (e.g., Melet et al., 2022).

In NEMOv3.6, the tidal energy flux E includes components for the M_2 , K_1 , and S_2 tides whereas Green and Huber (2013) provides an estimate only for the M_2 tide (see Figure S1 in Supporting Information S1 for a map of the estimated M_2 dissipation). Considering that (a) the M_2 component dominates the tide, and (b) the S_2 energy flux is simply taken to be $\frac{1}{4}$ of the M_2 energy flux in the NEMOv3.6 mixing scheme, we argue that using $\frac{5}{4}$ of the M_2 estimate of Green and Huber (2013) as forcing in the model ($M_2 + S_2$ contributions) is a reasonable first step, despite the missing K_1 contribution.

The two simulations are run for 5100 model years after which both have reached quasi-equilibrium with small residual trends in mean deep ocean (2,750–4,250 m) temperatures $<0.02^{\circ}\text{C}/\text{century}$ (Figure S2 in Supporting Information S1). The last 100 years of each model run are used to build a climatological average for the ocean dynamics. In order to improve the equilibration of biogeochemistry, we extend the simulations in an offline PISCES configuration for another 4000 model years. In this setup, the monthly mean climatological ocean dynamics is repeatedly read by PISCES to calculate the evolution of the biogeochemical tracer fields. Again, we use the last 100 model years to build a climatological average for the ocean biogeochemistry.

3. Results

3.1. Energetic Considerations

3.1.1. Available Energy

The tidal model used by Green and Huber (2013) yields an estimate of 1.44 TW of energy dissipated in the Eocene ocean by the M_2 barotropic tide, which, interpolated on the NEMO grid, amounts to 1.473 TW. Because the tidal mixing scheme in NEMO includes the S_2 tidal contribution expressed as one-fourth of the M_2 contribution, the total energy input from tides is 1.841 TW, of which only one-third, 0.614 TW, is assumed to dissipate locally and employed in the explicit tidal mixing scheme (because $q = \frac{1}{3}$ in Equation 1 above). The remaining two-thirds of tidal energy are assumed to dissipate in the far-field and are implicitly considered to be included in the background mixing.

The implementation of the tidal mixing scheme in the model is not fully consistent energetically for two reasons. First, a fraction of the energy input is lost in the lower half of the bottom cells, where stratification and diffusivity are not defined. Second, the model parameterization imposes an upper bound of $3 \times 10^{-2} \text{ m}^2 \text{ s}^{-1}$ on the tidal diffusivity (Madec et al., 2017).

We can diagnose the power consumption due to parameterized tidal mixing using the following equation, expressed as in S04:

$$P = \frac{1}{\Gamma} \int \rho(K_0 + K_{\text{Tides}})N^2 dV \quad (3)$$

Table 1 shows the amount of power consumed at the global scale and in each basin (Atlantic, Pacific, Indian, Tethys and Arctic, represented in Figure S3 of the Supporting Information S1). At the global scale, the total power consumed by tidal mixing in the model is 1.45 TW in EE-std. This is weaker than the 1.84 TW of total $M_2 + S_2$ tidal dissipation estimated by the model of Green and Huber (2013). Two considerations shed light on this difference. First, the effective consumption by near-field tidal mixing is only 0.42 TW, that is, about 70% of what is expected from Equation 1 (0.614 TW). Second, the background diffusivity is simply prescribed and does not depend on the tidal dissipation; hence power consumption by background mixing cannot be expected to match the unused two-thirds of barotropic tidal energy loss. However, Table 1 shows that local tidal mixing represents about 29% of the total power consumed by tidal mixing. This ratio is only slightly lower to that simulated by S04 in their modern experiments, but it means that the power consumption by background mixing (thought to represent other tidal mixing pathways) is close to two-thirds of the total, as already noted by S04. This is somewhat surprising given the very different paleogeography and stratification of our simulations. At the basin scale and excluding the Arctic basin, the contribution from near-field tidal mixing varies from 14% of the total power in the Tethys basin to 32% in the Pacific basin. This is consistent with larger mean barotropic tide dissipation rates in the Pacific and Indian Oceans than in the Atlantic and Tethys Oceans (Figure S1 in Supporting Information S1).

3.1.2. Diapycnal Diffusivity

The inclusion of tidal mixing substantially changes the amount of energy available to mix the deep ocean. Diapycnal diffusivities are therefore considerably different both horizontally and vertically in EE-std compared to EE-noM2.

In EE-noM2, the zonally averaged vertical diffusivity is generally close to the background value except in the surface mixed layer, in which mixing due to the winds generates elevated vertical diffusivity, and in the Southern Ocean where deep convection mixes waters down to the abyss (Figures 1a, 1c, and 1e). At mid depths (2,000–

Table 1
Power Consumed by Tidal Mixing and Fraction of Power Consumption Due To the Explicit Parameterization for Locally Dissipating Tides Calculated at the Global-Scale and for Individual Basins Shown on Figure S3 in Supporting Information S1

		Power consumption due to tidal mixing (TW)			Fraction of power consumption due to explicit local tidal mixing
		K_0	K_{Tides}	Total	
Global	EE-std	1.03	0.422	1.45	0.29
	EE-noM2	1.02	0	1.02	0
Pacific	EE-std	0.590	0.282	0.872	0.32
	EE-noM2	0.584	0	0.584	0
Atlantic	EE-std	0.162	0.056	0.218	0.26
	EE-noM2	0.160	0	0.160	0
Indian	EE-std	0.145	0.066	0.211	0.31
	EE-noM2	0.140	0	0.140	0
Tethys	EE-std	0.109	0.018	0.127	0.14
	EE-noM2	0.108	0	0.108	0
Arctic	EE-std	0.028	5×10^{-4}	0.028	0.02
	EE-noM2	0.026	0	0.026	0

Note. K_0 and K_{Tides} are defined in Section 2.2.

3,000 m), the zonal mean vertical diffusivity is elevated throughout the low latitudes (Figure 1a). This signal mostly originates from a relatively isolated abyssal sub-basin in the eastern Pacific Ocean between the East Pacific Rise and the American continent (Figure 1e) in which the weak stratification elevates K_{TKE} and stimulates episodic convective instabilities. At 600 m depth (Figure 1c), away from turbulent wind-driven mixing, vertical diffusivity is close to the background value K_0 except in deep convection zones of the Southern Ocean. Because the 600 m geopotential surface is also generally far from bottom topography, adding tidal mixing in EE-std does not significantly alter vertical diffusivity at this depth (Figure 1d), except in deep-water formation zones close to the Antarctic margins. By contrast, diffusivity at 3,000 m depth is enhanced by about 2 orders of magnitude in broad regions of the Pacific and Indian Oceans in EE-std relative to EE-noM2 (Figure 1f). Note that because tidal mixing is implemented here as a bottom-intensified energy dissipation, and because stratification generally decreases with depth, the maximum tidal diffusivity in the vertical is found locally on the deepest ocean grid cell. The Atlantic basin in the Eocene configuration exhibits a weaker tide than the Pacific (Green & Huber, 2013, see also Figure S1 in Supporting Information S1) and, therefore, vertical diffusivity does not increase as much as in the Pacific Ocean in EE-std compared to EE-noM2. The zonally averaged vertical diffusivity essentially shows that diapycnal mixing is substantially enhanced in the ocean interior. As we will show in the next sections, the additional mixing energy available in the deep ocean has profound consequences on the intensity of the overturning circulation and the pathways of water masses.

3.2. Surface Changes

The upper-ocean (0–100 m) annual mean temperatures in EE-noM2 are roughly close to 10°C in the Southern Ocean and to 5°C in the quasi-enclosed Arctic Ocean (Figure 2a). They increase equatorward to reach up to more than 37°C in the equatorial western Pacific. As expected from similar simulations performed with the same model, this temperature distribution is very close to that presented in Figure 2a of Zhang et al. (2020) (see Figure S4 in Supporting Information S1 for a more detailed comparison). Tidally driven mixing leads to large changes in the Southern Ocean surface layer. The Atlantic and Indian sectors of the Southern Ocean are warmer (locally more than 4°C) in EE-std than in EE-noM2 (Figure 2b), whereas the Pacific sector is cooler, although the change is smaller. Warmer (cooler) regions of the Southern Ocean in EE-std are also regions of increased (decreased) upper ocean salinity due to local increase in evaporation (not shown).

In EE-noM2, deep convective areas are exclusively found in the Southern Ocean, in the Atlantic, Indian and Pacific sectors (Figure 2c), and there is no deep-water formation in the Northern Hemisphere. The upper-ocean

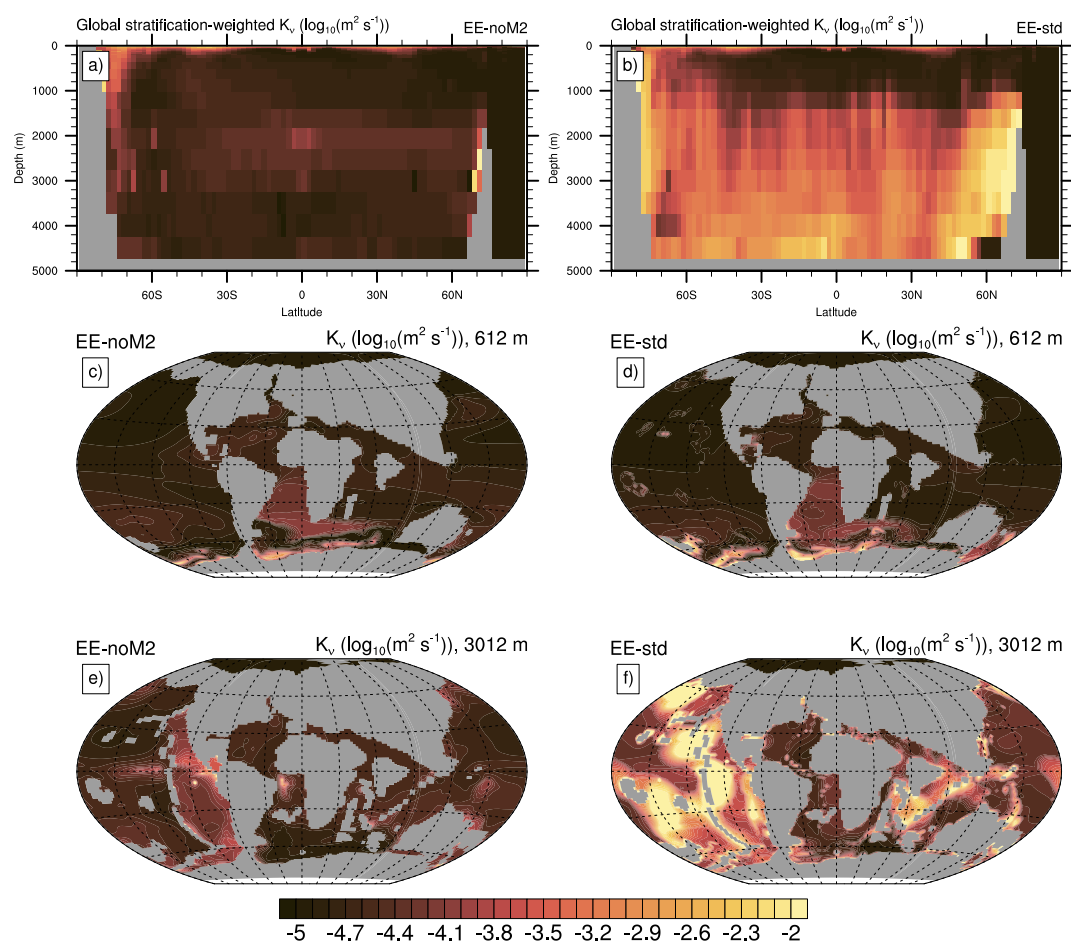


Figure 1. Stratification-weighted global zonal average of vertical diffusivity for EE-noM2 (a) and EE-std (b) ($\log_{10}(\text{m}^2 \text{s}^{-1})$). Diffusivity at 600 and 3,000 m for EE-noM2 (c, e) and EE-std (d, f) ($\log_{10}(\text{m}^2 \text{s}^{-1})$).

temperature changes in EE-std are sustained by increased deep-water formation in the Atlantic and Indian sector of the Southern Ocean compared to EE-noM2 as can be seen by the deepening of the winter mixed layer depth (MLD) in these areas (Figure 2d). In the South Atlantic, the MLD deepens by more than 1,000 m and enhances the temperature and salt advection feedback from the lower latitudes. In the Pacific sector, the winter MLD instead slightly decreases, driving the opposite change in the advection feedback. Figure S5 in Supporting Information S1 further shows that the deepening/shoaling of MLD in EE-std relative to EE-noM2 is robust across the simulations and not simply an artifact of the averaging period.

3.3. Ocean Circulation Changes

The increase in available energy for mixing is reflected by a significant enhancement of the global MOC (Figure 3). The MOC in the two simulations has a roughly comparable shape consisting of a single anticlockwise overturning cell in the Southern Hemisphere fed by deep-water formation in the Southern Ocean. The intensity of the MOC and the penetration of deep-water in the abyss is however greater in EE-std than in EE-noM2, although the maximum rate of overturning is similar in the two simulations (~ 35 Sv at 2,000 m depth in EE-std and at 900 m depth in EE-noM2). Away from the Southern Ocean, the additional tidal mixing energy sustains a stronger and deeper overturning cell extending up the northern mid to high latitudes (8 Sv at 2,000 m depth and 30°N in EE-std, Figure 3b), effectively increasing the ventilation of the EE-std ocean compared to EE-noM2 and acting to reduce vertical tracer gradients.

This homogenization is evident from the global zonal mean distribution of temperature (Figure S6 in Supporting Information S1), which shows a globally warmer deep ocean (below $\sim 1,000$ m) and a globally cooler upper and

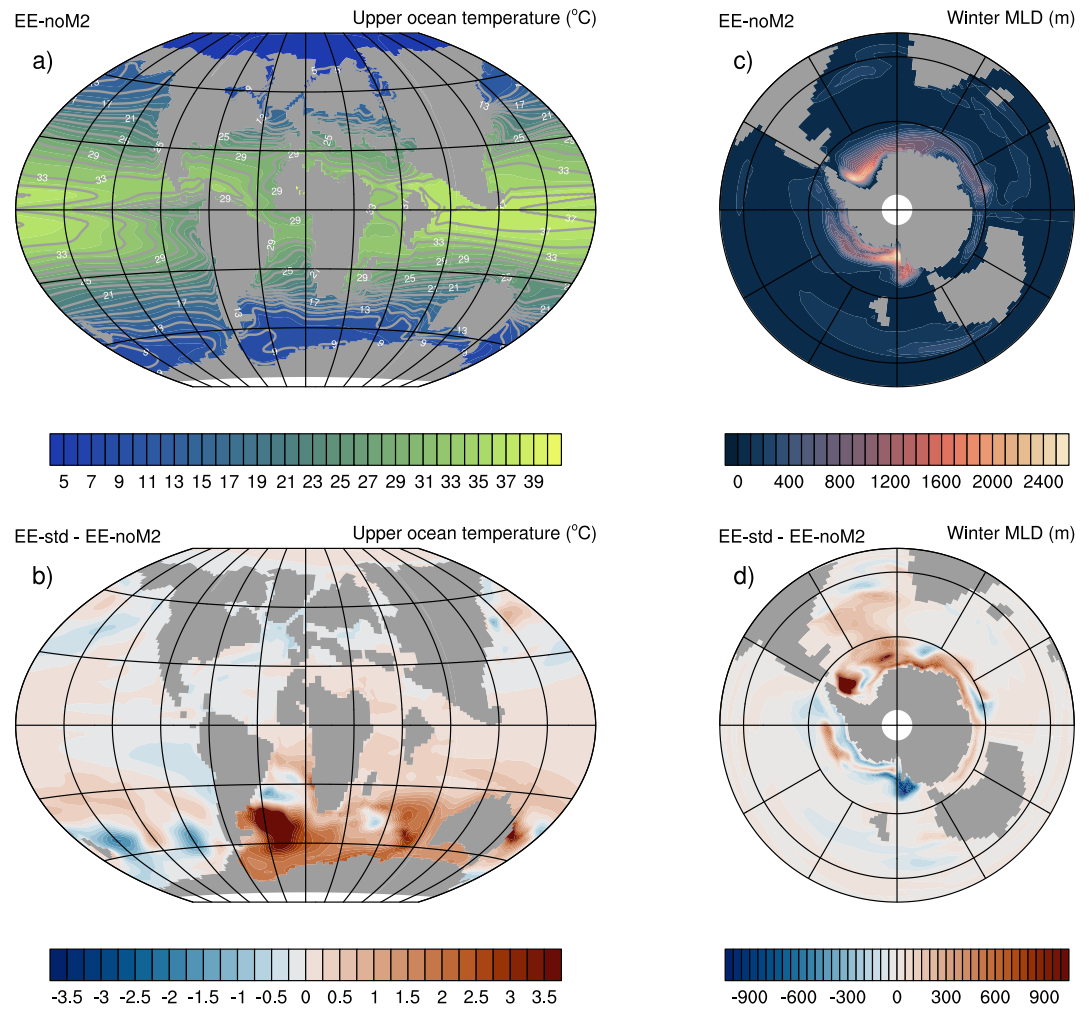


Figure 2. (a) EE-noM2 mean annual upper ocean (0–100 m) temperatures (°C). (b) Mean annual upper ocean temperature (0–100 m) difference (°C) between EE-noM2 and EE-std. (c) Mean winter MLD (m) in EE-noM2. (d) Mean winter MLD difference (m) between EE-std and EE-noM2.

intermediate ocean in EE-std compared to EE-noM2 at all latitudes except those of the Southern Ocean (80°S–40°S) where the ocean is globally warmer throughout the water column. The EE-std ocean is thus more vertically well mixed than the EE-noM2 ocean, consistent with substantially larger global mean vertical diffusivities below 1,500 m depth in EE-std relative to EE-noM2 (Figure S7 in Supporting Information S1).

The intensification of the global MOC has interesting consequences on the water mass pathways, in particular in the Atlantic. Figure 4 shows the ocean current velocity and direction at different depths in the South Atlantic and Southern Ocean. At 500 m depth, the western boundary current flowing southward off the coast of South America is substantially increased in EE-std. As a consequence, the westward-flowing water masses offshore Antarctica remain confined to the Southern Ocean, whereas in EE-noM2, these waters flow northward around the tip of South America and mix with the southward-flowing waters of the South Atlantic western boundary current before flowing toward the Indian Ocean (Figures 4a and 4b). Deeper in the water column (1,400–1,800 m depth), the water masses flowing from the Atlantic to the Indian sector of the Southern Ocean in EE-noM2 consist of recirculated waters from the Southern Ocean and locally formed deep waters, as the southward-flowing Atlantic western boundary current is absent. In contrast, in EE-std, the southward western-boundary current is still active and contributes to exporting water masses from the low-latitude Atlantic toward the Indian Ocean (Figures 4c and 4d). In the abyss (3,250–3,750 m), only a very small fraction of the Southern Ocean water masses flows northward in the Atlantic in EE-noM2 while most are exported eastward to the Indian Ocean. In EE-std an intense northward

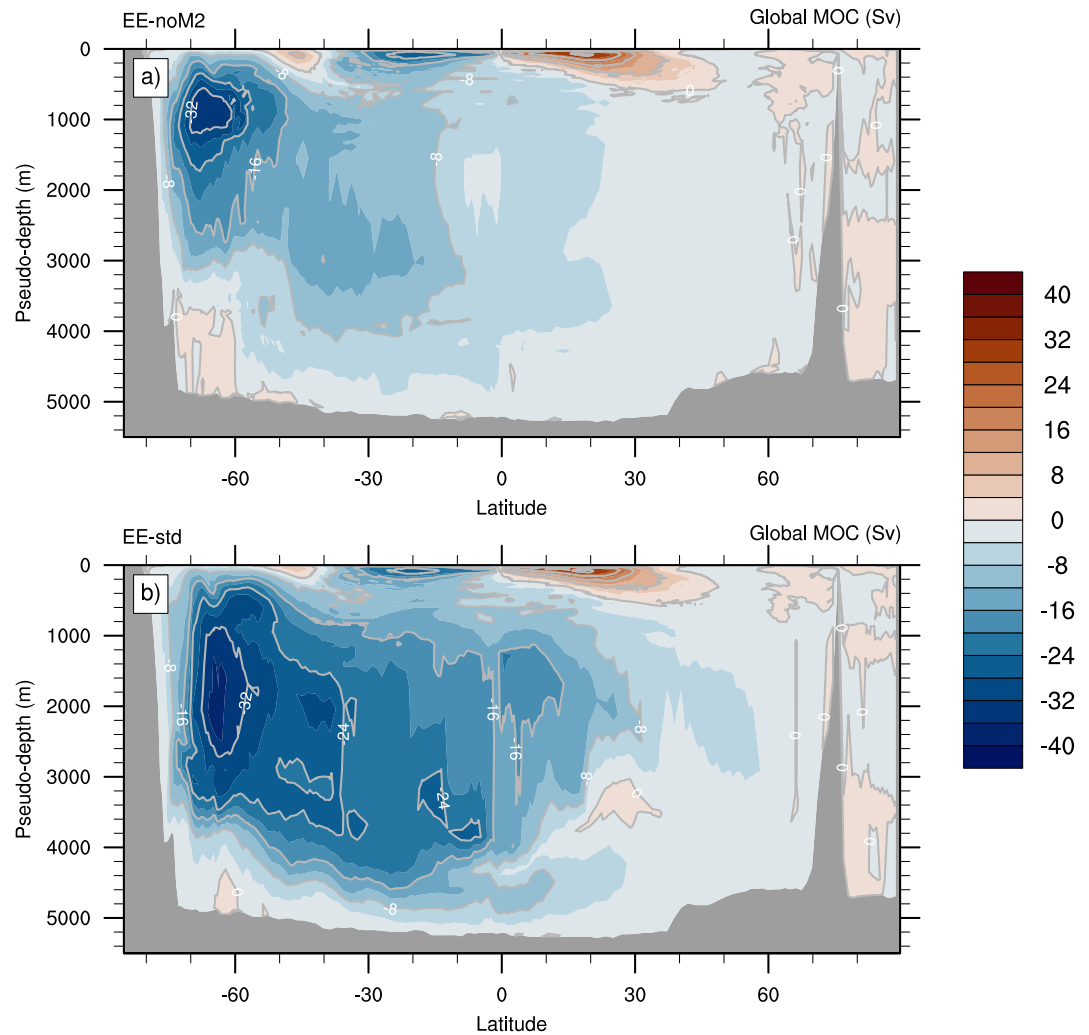


Figure 3. Global meridional overturning streamfunction (Sv) in EE-std (a) and EE-noM2 (b). Note that the MOC has been computed in density coordinates and reprojected to a pseudo-depth, following de Lavergne et al. (2017).

current advects water masses along the western side of the basin into the Equatorial and North Atlantic (Figures 4e and 4f).

These results demonstrate that the deep Equatorial and North Atlantic Oceans are more isolated from the global ocean circulation below $\sim 1,500$ m in EE-noM2 than in EE-std. In the Early Eocene, the deepest connections of the Atlantic basin are with the Southern Ocean because the Central American, Tethys (Gibraltar) and Atlantic-Arctic gateways are all shallow and/or narrow. Since the bathymetric configuration does not change between the two simulations, the increased isolation of the EE-noM2 Equatorial and North Atlantic Oceans is purely caused by lower levels of deep turbulent mixing, leading to major differences in Atlantic stratification and circulation. In EE-std, tidal mixing renders abyssal water masses increasingly more buoyant as they flow away from deep-water formation areas in the Southern Ocean whereas the buoyancy gain across the Atlantic is weaker in EE-noM2. The isopycnal located at approximately 3,000 m depth at 45°S (the 40.08 and 39.98 $\text{kg m}^{-3} \sigma_3$ contour in EE-noM2 and EE-std respectively, Figure 5) indeed deepens to about 3,400 m depth in EE-noM2 and 4,500 m depth in EE-std at 35°N . In other words, isopycnals of similar depth in the deep South Atlantic exhibit depth differences in excess of 1 km upon reaching the deep North Atlantic. The larger northward deepening of the isopycnals across the deep Atlantic generates a stronger meridional pressure gradient and, thus, forces a more active deep northward circulation (e.g., Whitehead, 1998) in EE-std compared to EE-noM2, leaving the latter more stagnant.

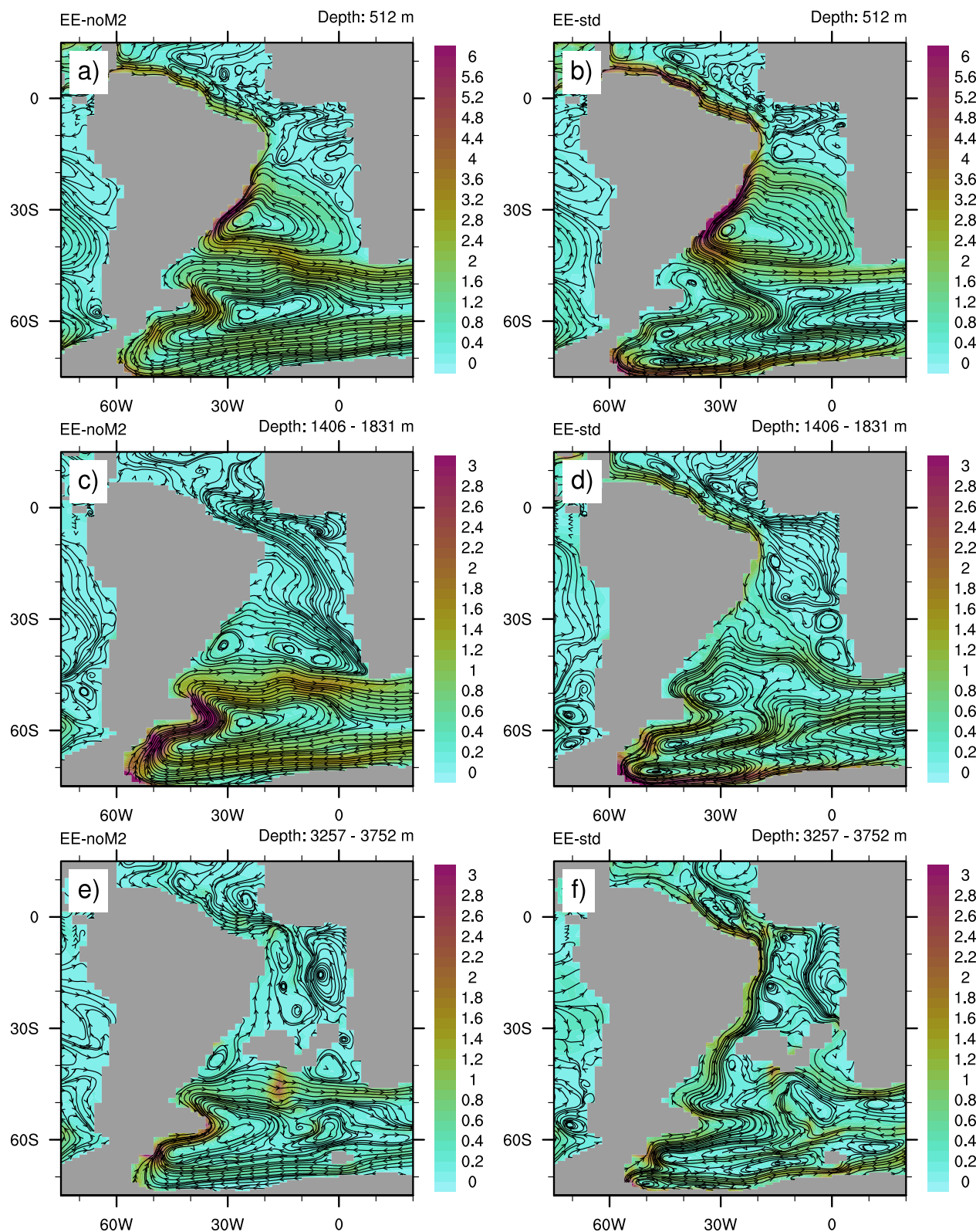


Figure 4. Ocean velocity (cm s^{-1}) at 500 m depth (a, b), averaged between 1,400 and 1,800 m (c, d) and averaged between 3,250 and 3,750 m (e, f) in EE-noM2 (a, c, e) and EE-std (b, d, f).

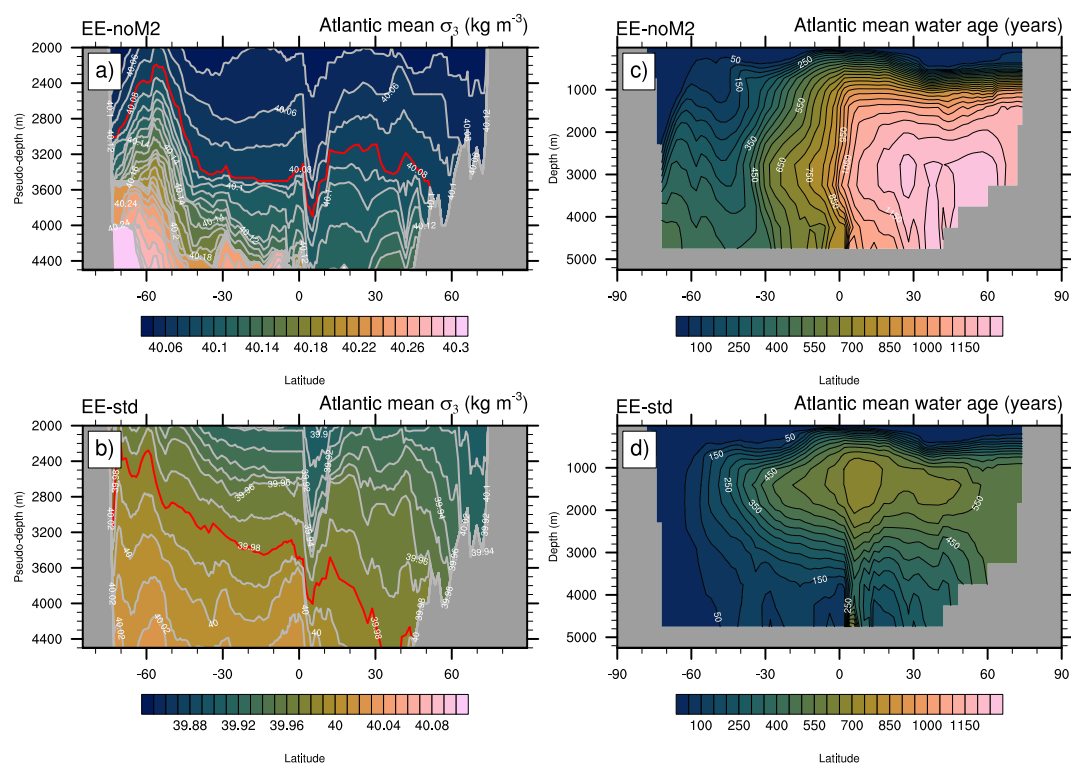


Figure 5. Zonally averaged σ_3 isopycnal profiles (kg m^{-3}) across the deep Atlantic in EE-noM2 (a) and EE-std (b) computed in density coordinates and reprojected to a pseudo-depth. The 40.08 and 39.98 kg m^{-3} σ_3 contours are highlighted in red in (a) and (b) respectively, for easier visualization. Zonally averaged water age profile across the Atlantic in EE-noM2 (c) and EE-std (d). Note the different vertical axes between the two columns.

3.4. Biogeochemical Changes

The more active deep circulation with tidal mixing also yields a significant reorganization of the marine biogeochemistry in the deep ocean, in particular in the Atlantic. At the global scale, though it is once again more evident in the Atlantic (Figures 5c and 5d), the deep ocean ventilation is reduced in the absence of tidal mixing. Notably, deep North Atlantic water masses are almost 3 times older in EE-noM2 than in EE-std. These deep water masses therefore exhibit very different biogeochemical properties in EE-noM2 and EE-std, and this is particularly visible on the distribution of dissolved oxygen across the water column.

In EE-noM2, the deep North Atlantic water masses possess the biogeochemical signature of very old water masses: rich in nutrients and dissolved inorganic carbon (DIC) and poor in oxygen. In fact, the North Atlantic is spectacularly oxygen-depleted (Figure 6a), with hypoxia (defined here as the 62.5 mmol m^{-3} level) reached over the whole water column in the low latitudes of the North Atlantic (0–20°N) and below 800 m northward of 30°N. Anoxic levels are reached northward of 20°N at depths between 1,500 and 3,000 m. The North Atlantic seafloor is fully hypoxic and most of the coastal seafloor is anoxic (Figure 6c). In contrast, deep North Atlantic DIC and phosphate concentrations are high (Figures S8 and S9 in Supporting Information S1) because falling organic matter has been remineralized along the water mass journey and nutrients have therefore accumulated in the deep ocean. Nitrate concentrations, however, rather decrease northward in the deep Atlantic (Figure S10 in Supporting Information S1) because the depletion in oxygen in this ocean basin triggers denitrification to continue the remineralization process.

In EE-std, the younger water masses in the deep North Atlantic are relatively rich in oxygen (Figure 6b) and the seafloor is well oxygenated with only very limited hypoxic coastal areas. The North Atlantic exhibits higher nitrate concentrations in EE-std than EE-noM2 in the deep (Figure S10 in Supporting Information S1), because the oxygen levels are above those required to trigger denitrification, and we find lower DIC and phosphate concentrations (Figures S8 and S9 in Supporting Information S1), as expected for better ventilated water masses.

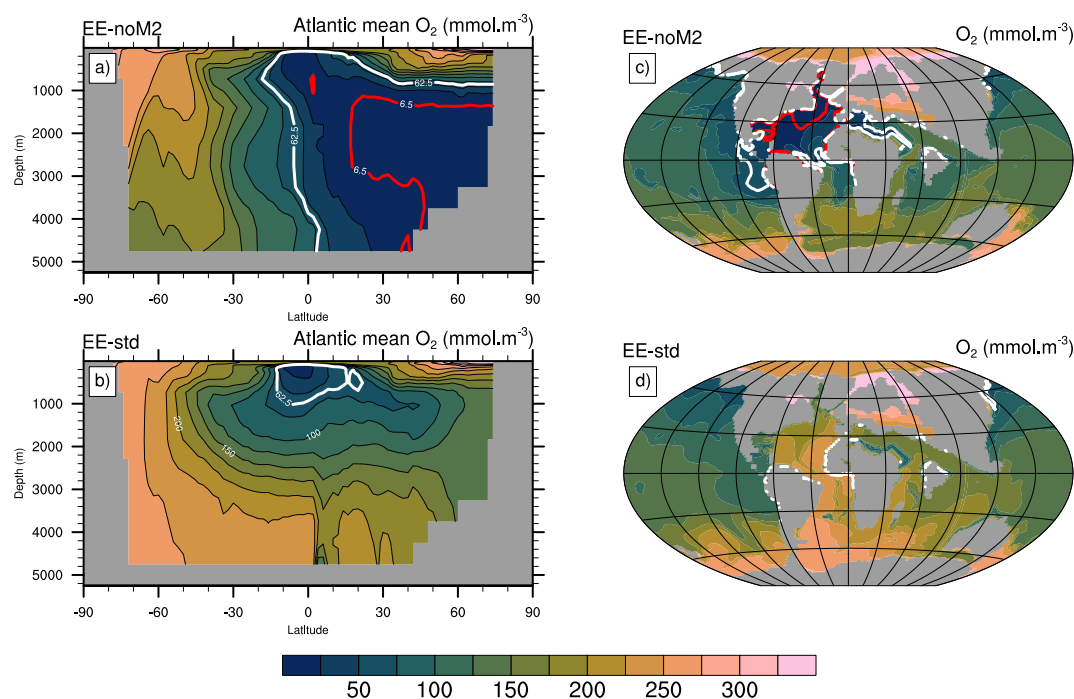


Figure 6. Zonally averaged dissolved oxygen concentrations (mmol m^{-3}) across the Atlantic in EE-noM2 (a) and EE-std (b). Dissolved oxygen concentrations (mmol m^{-3}) at the seafloor in EE-noM2 (c) and EE-std (d). The hypoxic (62.5 mmol m^{-3}) and anoxic (6.5 mmol m^{-3}) thresholds (Laugié et al., 2021) are contoured in white and red, respectively.

There are three main processes controlling the oxygenation of water masses in the ocean: surface atmosphere-ocean interaction controlling the degree of solubility of O_2 in the ocean, ocean circulation, and biological activity. Dissolved O_2 concentrations in the ocean can be decomposed into a thermal and a non-thermal component, referred to as the saturation component ($\text{O}_{2\text{sat}}$) and the Apparent Oxygen Utilization (AOU) respectively. $\text{O}_{2\text{sat}}$ is the concentration of O_2 that can be dissolved for a given temperature and salinity whereas AOU integrates the contribution of ocean circulation and biology. These quantities are related through:

$$\text{O}_2 = \text{O}_{2\text{sat}} - \text{AOU}$$

As shown in Figure 7 for EE-noM2, surface $\text{O}_{2\text{sat}}$ increases poleward because solubility increases with decreasing temperatures (Figure 7b). Surface O_2 concentrations are generally close to $\text{O}_{2\text{sat}}$ because, besides interacting with the atmosphere, the upper ocean layers gain dissolved O_2 as the result of photosynthesis of marine phytoplankton. The AOU is therefore low (e.g., the surface mid-latitudes in Figure 7c). One notable exception is the equatorial subsurface ocean because it is a region of upwelling that brings to the upper ocean water masses extremely rich in nutrients allowing for intense phytoplanktonic activity. Consequently, large amounts of organic matter sink and consume oxygen at a rate faster than the one at which the ocean restores its O_2 concentration by atmospheric exchange.

In the intermediate and deep ocean, O_2 concentrations are close to $\text{O}_{2\text{sat}}$ in the Southern Ocean where deep convection occurs (Figures 7a and 7b). As water masses age in the ocean interior (Figure 7d), O_2 concentrations depart from $\text{O}_{2\text{sat}}$ because of the increasing influence of remineralization processes that consume oxygen in the water column (reflected by the increasing AOU, Figure 7c). In the deep North Atlantic, extremely old water masses that have not been in contact with the atmosphere for more than a millennium exhibit AOU values almost equal to $\text{O}_{2\text{sat}}$, indicating that almost all the available O_2 has been consumed.

Any change in dissolved O_2 concentrations between EE-noM2 and EE-std can therefore be partitioned into the change in $\text{O}_{2\text{sat}}$, reflecting the change in temperature and, to a lesser extent, salinity between EE-std and EE-noM2 and the change in AOU, which reflects circulation and biological changes:

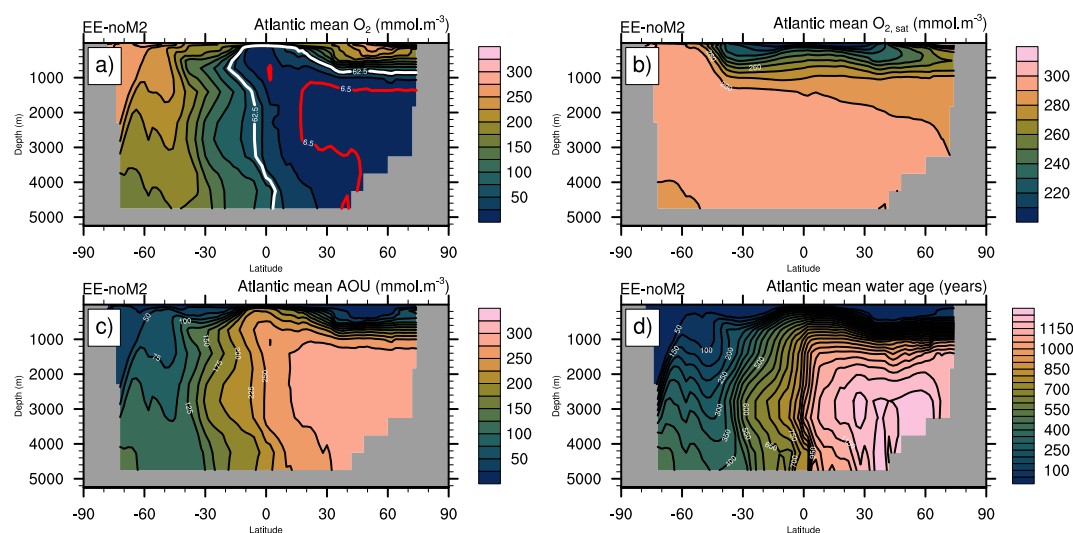


Figure 7. Zonally averaged (a) dissolved oxygen concentrations (mmol m^{-3}), (b) $\text{O}_{2\text{sat}}$ (mmol m^{-3}), (c) AOU (mmol m^{-3}) and (d) water age (years) across the Atlantic in EE-noM2. Note the different scale in panel (b) relative to (a) and (c).

$$\Delta\text{O}_2 = \Delta\text{O}_{2\text{sat}} - \Delta\text{AOU}$$

In the Atlantic, the changes in dissolved O_2 concentrations are almost fully explained by changes in AOU (Figure 8). Interestingly, Figure 8 shows that contours of ΔAOU and of the water age difference between EE-std and EE-noM2 are very well correlated, thereby strongly hinting that the primary driver of oxygen changes is the reorganization of the ocean circulation following the addition of tidally driven mixing. This is also confirmed by the limited changes in export productivity to the intermediate and deep ocean (Figure S11 in Supporting Information S1).

4. Discussion

Our simulations demonstrate the crucial role played by tidally driven abyssal turbulent mixing in shaping the circulation and the distribution of biogeochemical tracers in the ocean interior. However, apart from a few sensitivity simulations (Hutchinson et al., 2018; Thomas et al., 2014), most earth system models applied to deep-time climates generally neglect tidally driven mixing as a specific forcing and alter (or not) spatially constant coefficients in the implemented vertical mixing parameterization (e.g., Bryan & Lewis, 1979) as a workaround (e.g., Zhang et al., 2022). In the following, we first briefly discuss our results in the context of similar work performed on modern climates, then of DeepMIP simulations and of the few studies that have investigated the climatic effects of tides in deep-time paleoclimates. We stress however that no previous deep-time paleoclimate simulation is exactly comparable to the simulations presented here because of differences in model parameterizations or in the implemented tidal physics. In a second time, we compare our biogeochemical results to previous biogeochemical model studies and the proxy record of ocean oxygenation in the Early Eocene.

There is, to our knowledge, no thorough comparison between a constant background diffusivity and the S04 parameterization in deep-time paleoclimate simulations, but such comparison has been made in the context of modern climates (Jayne, 2009; Saenko & Merryfield, 2005). In particular, the low-resolution simulations of Jayne (2009) show little sensitivity of the intensity of global MOC to the addition of tidal mixing compared to the constant background case (the AMOC increases by ~ 1 Sv while the abyssal MOC decreases by ~ 0.5 Sv) although the locus of maximum abyssal MOC is shifted equatorward in the tidal mixing simulation (Figure 4 of Jayne (2009)). Saenko and Merryfield (2005) also observe little impact of the addition of tidal mixing on the intensity and structure of the AMOC. This contrasts with our simulations in which the MOC in EE-std penetrates deeper and extends further in the Northern Hemisphere (Figure 3). The difference in sensibility of the simulated circulation to tidal mixing between the Early Eocene and the modern may be rooted in the paleogeography. In the modern ocean, deep waters upwell along isopycnals in the Southern Ocean under the combined action of winds

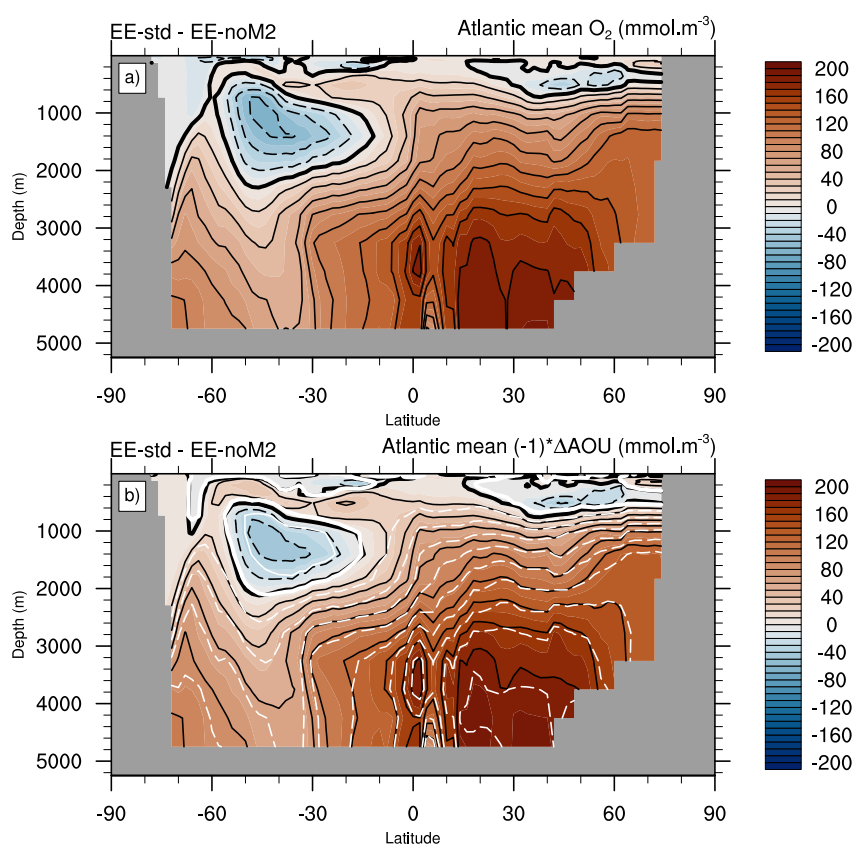


Figure 8. Zonally averaged (a) dissolved oxygen concentration difference (mmol m^{-3}) and (b) AOU difference (mmol m^{-3}) across the Atlantic between EE-std and EE-noM2 (shading and black contours). White contours denote the difference in water age between EE-std and EE-noM2 (positive solid and negative dashed).

and eddies in the Antarctic Circumpolar Current (ACC) system (e.g., Marshall & Speer, 2012). In contrast, the absence of ACC in the Early Eocene, due to very restricted configurations of the Drake Passage and Tasman Gateway, implies that diapycnal abyssal mixing is the only way to remove waters from the deep ocean (e.g., Green & Huber, 2013).

As noted in the Introduction and touched upon in Zhang et al. (2022), there is no consistency among the models that participated in DeepMIP in terms of parameterizations of abyssal mixing and the intensity of the overturning does not necessarily scale with the intensity of abyssal mixing rates. The 840 ppmv CO₂ simulations of IPSL-CM5A2, MIROC and CESM have the strongest overturning intensity (~ 16 Sv at 3,000 m depth) and, while IPSL-CM5A2 includes a tidal mixing scheme (as in EE-std), MIROC and CESM have BL profiles with large diffusivity coefficients in the deep ocean (Zhang et al., 2022, and references therein). This would suggest that these two models incorporate the basic effects of Early Eocene tidal mixing and might not display significant sensitivity to the inclusion of an explicit tidal mixing scheme, unless the spatial variability of tidal dissipation exerts a primary influence on the simulated deep ocean circulation (but this remains to be explored). In contrast, COSMOS has a uniform background diffusivity coefficient (as in EE-noM2) and effectively produces weaker overturning (~ 8 Sv at 3,000 m depth). However, HadCM3B, GFDL-CM2.1, and NorESM do not fit in this simple view. The NorESM simulation is indeed inconclusive because probably still in the spin-up phase, as suggested by a warming deep ocean (Figure S2 of Zhang et al. (2022)). HadCM3B shows similar rates of overturning as COSMOS although the prescribed background diffusivity increases with depth and, in this sense, is comparable to the coefficients given by a BL profile. One possible reason could be that HadCM3B seems to produce weaker deep-water formation compared to other models, as shown by the winter mixed-layer depths in Figure 2 of Zhang et al. (2022), perhaps due to stronger restratification processes. GFDL includes the S04 tidal mixing scheme (as IPSL-CM5A2) but exhibits weaker overturning intensity (~ 8 Sv at 3,000 m depth). Whether this is related to the fact that GFDL is the only model producing deep water formation essentially in the North Pacific rather than the

Southern Ocean, and/or to the specifics of the parameterized tidal mixing implementation or to other aspects of the model configurations, remains unknown at the moment.

Hutchinson et al. (2018) analyze, among others, two 840 ppmv CO₂ GFDL-CM2.1 Late Eocene simulations that differ by the vertical diffusivity scheme employed in the ocean interior, being either the standard **BL** profile or the tidal mixing parameterization of **S04**. The global MOC in the **BL** simulations shows a two-cell structure in the deep ocean in which the upper cell is fed by North Pacific waters and the bottom cell by Southern Ocean waters. Switching to the **S04** scheme only negligibly affects the simulated MOC, whose intensity is comparable to those found in the “intense overturning” models of DeepMIP (i.e., ~16 Sv at 3,000 m depth). This prompts the suggestion that the weaker intensity found in the GFDL DeepMIP simulation might be partly explained by the absence of deep overturning fed by Southern Ocean dense water formation. The insensitivity of the GFDL Late Eocene simulations of Hutchinson et al. (2018) to the mixing scheme also adds support to the idea that the bottom-intensified **BL** profile accounts for the basic effects of tidal mixing—although without spatial dependence—and, as such, that the impact of including an explicit near-field tidal mixing may be largely mitigated. Figure 9 of Hutchinson et al. (2018) indeed shows that the stratification-weighted global mean diffusivity profile is quasi-identical in the first 4,000 m in their **BL** and **S04** simulations, which markedly contrasts with our Figure S7 in Supporting Information S1 showing that the global diffusivity differs by at least one order of magnitude below 1,500 m in EE-std relative to EE-noM2. However, we note that, comparing the **BL** and **S04** schemes in a modern configuration of the same resolution as Hutchinson et al. (2018) and Jayne (2009) observes a ~30% increase in the intensity of the deep cell of the MOC in **S04** with little change in MOC structure, implying that the details of the implementation of the tidal mixing scheme may also impact the simulated circulation. In Hutchinson et al. (2018), the input dissipation rate *E* is recomputed directly using Equation 2 of **S04** and a uniform seafloor roughness amplitude and it is possible that the latter may smooth out the spatial variability in tidal energy dissipation. Alternatively, (a) the change in tidal forcing between the Late Eocene and the modern, (b) a different sensitivity of the Late Eocene circulation to tides compared to the modern, or (c) different levels of spurious numerical mixing in GFDL-CM2.1 and CCSM3 (e.g., Holmes et al., 2021) may concur to explain the discrepancies between the results of Hutchinson et al. (2018) and Jayne (2009). This nonetheless suggests that the spatial distribution of the tidal forcing has the potential to alter the simulated ocean circulation (Jayne, 2009; Saenko, 2006).

In ocean-only MITgcm simulations of the Early Eocene, which includes an older reconstruction of the paleogeography compared to the DeepMIP one used here, Thomas et al. (2014) explored the sensitivity of the ocean circulation to various **BL**-type profiles for the background vertical mixing. Though these experiments do not explicitly include tidal mixing, those with enhanced abyssal mixing can be seen as surrogates to investigate the effect of more intense tides because tides are the primary supplier of mixing in the deep ocean. Thomas et al. (2014) found that increasing the diffusivity beyond the standard **BL** coefficients allows for a large increase in the intensity of the MOC and yields a circulation mode that compares better to compiled Pacific ϵ_{Nd} data, in particular in the case in which abyssal mixing is increased. In this latter case, the intensity of the overturning is more than tripled for a more than fivefold increase in the background diffusivity coefficient in the deep ocean. Thomas et al. (2014) however note that the increased abyssal mixing does not markedly affect the OHT, (whereas an increase in the upper ocean diffusivity does). This analysis is in agreement with the results of previous investigations of the effect of ocean mixing on OHT (e.g., Ferrari & Ferreira, 2011; Jayne, 2009), which notably demonstrate that increasing deep ocean mixing enhances mass but not heat transport because of the small temperature difference in the deep ocean (Ferrari & Ferreira, 2011). Accordingly, the meridional SST gradient in our simulations is only weakly affected by the addition of tidal mixing because vertical diffusivity in the upper 1,000 m is similar in EE-noM2 and EE-std (Figure S7 in Supporting Information S1). Below 1,000 m, diffusivity (and mass transport) increases substantially in EE-std but the vertical temperature gradient does not (Figure S6 in Supporting Information S1) and the change in heat transport is small.

Using the ECHAM5/MPIOM model with the Early Eocene paleogeography of Heinemann et al. (2009) and Weber and Thomas (2017) investigated the response of the Eocene ocean circulation to tides. They simulate the change in ocean circulation in a similar setup than the one presented here, but the physics of the tides included in their model are fundamentally different than that discussed in our simulations. Specifically, Weber and Thomas (2017) account for tidal residual currents by including an explicit tidal forcing on the momentum equations, rather than for near-field tidal mixing. The simulated ocean circulation of Weber and Thomas (2017) exhibits deep-water formation in the Southern Atlantic, as here, but also in the North Atlantic. Adding the tidal influence of residual tidal currents does not substantially modify the location of deep-water formation regions but

does change the depth of deep convection, although the limited integration time of their tidal simulation (100 years) prompts the possibility that it might not have reached sufficient equilibrium. One possible reason, among others (see, e.g., Zhang et al., 2022), explaining the different regions of deep convective activity is the paleogeographic reconstruction: in Weber and Thomas (2017), it features a closed Drake Passage and Tasman Gateway and a more widely opened Central American Seaway compared to the Herold et al. (2014) DeepMIP reconstruction that we use. Weber and Thomas (2017) report an increase in the intensity of the MOC but hardly any increase in ocean heat transport, in keeping with the notion that the impacts of the Eocene tides are concentrated in the abyssal ocean (Green & Huber, 2013). Although the details of the ocean circulation differ between our simulations and those of Weber and Thomas (2017), and although the impact of tides is implemented as residual tidal currents rather than as a diffusive mixing term, there are similar effects on the simulated MOC in their experiments and ours.

From a biogeochemical perspective, other studies have attempted to simulate the biogeochemical state of the Early Eocene (e.g., Heinze & Ilyina, 2015), generally in order to focus on the PETM perturbation (Ilyina & Heinze, 2019; Meissner et al., 2014; Winguth et al., 2012). In particular, Winguth et al. (2012) and Heinze and Ilyina (2015) have used modeling setups consisting of biogeochemical models of resolution and complexity similar to PISCES and forced by or coupled to ocean-atmosphere GCMs, but the prescribed paleogeography and atmospheric CO₂ bear no consistency between the studies, unlike more recent coordinated efforts such as DeepMIP (Lunt et al., 2017, 2021). Deep O₂ concentrations exhibit large differences between the simulations: the 1,120 ppmv CO₂ simulation of Winguth et al. (2012) generates a well oxygenated Pacific Ocean and a more poorly oxygenated Atlantic Ocean whereas the 560 ppmv CO₂ simulation of Heinze and Ilyina (2015) shows a better oxygenated Atlantic than Pacific Ocean. In our simulations with tidal mixing at 840 ppmv, the deep Atlantic is better oxygenated than the Pacific (Figure S12 in Supporting Information S1) but the equatorial Atlantic oxygen minimum zone is more developed and has lower O₂ concentrations. Interestingly, the primary production patterns in the upper ocean are more alike, with for instance intense primary production in most of the equatorial Pacific, in the eastern side of the Pacific and Atlantic Oceans, as well as in the Southern Ocean. This suggests that the diversity in O₂ distributions across the simulations largely reflects the simulated ocean circulation, at least in the deep ocean.

There is currently no quantitative proxy for O₂ concentrations in the past, although semi-quantitative multi-proxy approaches can provide estimates of poorly oxygenated bottom water conditions ($\leq 50 \mu\text{mol kg}^{-1}$) (Lu et al., 2020). Most studies therefore report qualitative estimates of the local oxygenation state of the ocean relative to a baseline value, using redox-sensitive proxies such as the I/Ca ratio (e.g., Zhou et al., 2014, 2016), trace elements like molybdenum or manganese (Dickson et al., 2012, 2014; Pälke et al., 2014) or magnetofossils (Xue et al., 2022, 2023). Anoxic bottom water masses are perhaps more easily identifiable because the sedimentary abundance of trace elements is strongly redox dependent and sedimentary enrichment above average crustal values via complexification with sulfide elements is interpreted as reflecting high dissolved sulfide concentrations and thus anoxic/euxinic conditions (Dickson et al., 2012, 2014). If the distribution of Early Eocene redox archives is relatively global (though concentrated in the peri-Tethys area, see Figure 6 of Carmichael et al. (2017)), the information conveyed by these estimates remains potentially strongly influenced by local settings (Clarkson et al., 2021). A complementary approach therefore consists in estimating the global area or volume occupied by anoxic or euxinic waters, using the isotopic ratio of molybdenum (Dickson et al., 2012), sulfur (Yao et al., 2018) or uranium (Clarkson et al., 2021), rather than reporting local estimates of bottom water oxygenation. For instance, combining uranium isotope measurements from ODP Site 865 (Allison Guyot, equatorial Pacific Ocean), DSDP Site 401 (Bay of Biscay, northeast Atlantic Ocean) and ODP Site 690 (Maud Rise, Atlantic sector of Southern Ocean) with box modeling, Clarkson et al. (2021) propose a maximal extent of seafloor anoxia of 0.25% prior to the PETM perturbation and 2% at the PETM.

In the following, we compare the simulated oxygen concentrations in EE-noM2 and EE-std with available data across a transect in the Atlantic using reported oxygen conditions at each site (Figure 9) and compute the extent of anoxic seafloor simulated by the model. Three main observations can be made. First, the qualitative nature of the proxy leaves room for various interpretations. At the exception of Site 1262 and 1266 at Walvis Ridge for whose oxygen-rich conditions have been reported by the different proxies (Pälke et al., 2014; Xue et al., 2022), low oxygen content is estimated at every site but the degree of oxygen deficiency is unclear because anywhere between the anoxic ($0 \mu\text{mol L}^{-1}$) and hypoxic threshold ($\sim 60\text{--}70 \mu\text{mol L}^{-1}$, Laugié et al., 2021; Lu et al., 2020). Second, at face value, the simulated O₂ concentrations are probably too low in EE-noM2, in particular in the

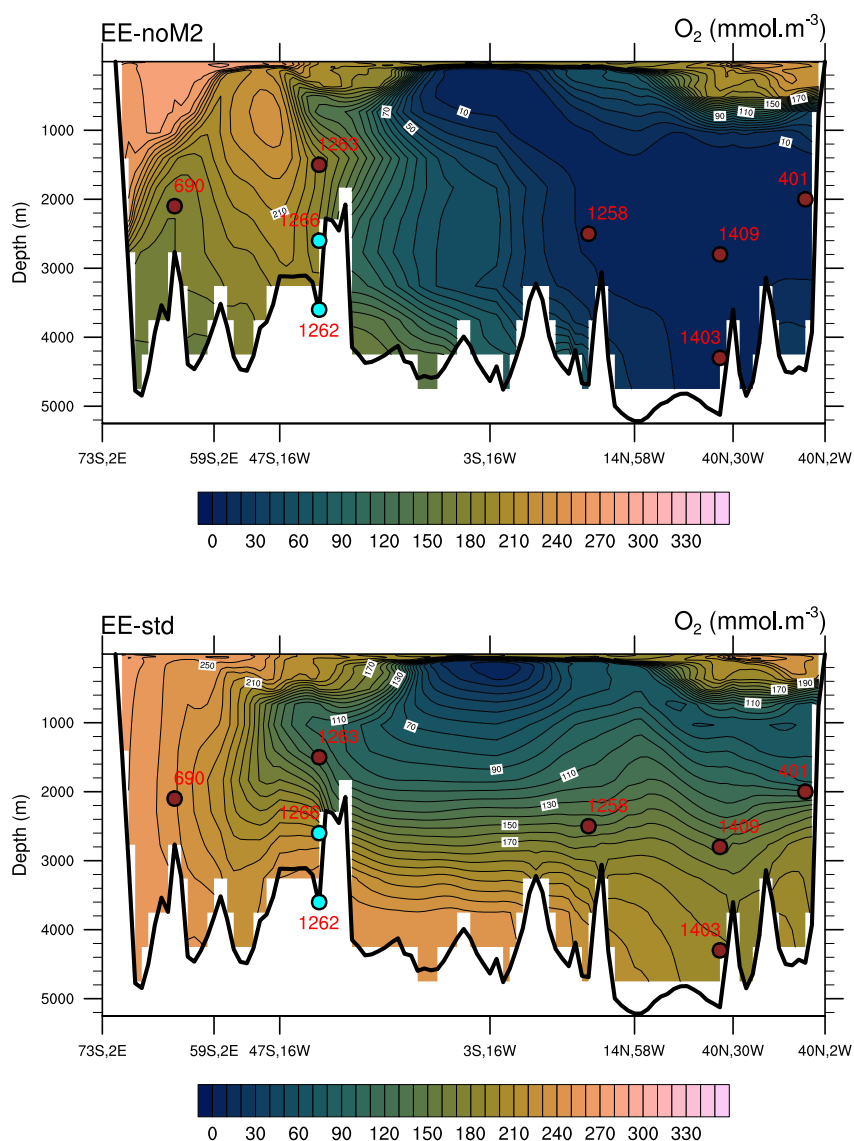


Figure 9. Dissolved oxygen concentration (mmol m^{-3}) transect across the Atlantic for EE-noM2 (a) and EE-std (b). The transect followed is shown on Figure S3 in Supporting Information S1. At the exception of Sites 1262 and 1266 (blue color), for which oxygen-rich conditions have been reported, other Atlantic sites (brownish color) exhibit low oxygen conditions, according to proxy data.

North Atlantic, and too high in EE-std. Third, the fact that reported qualitative oxygen conditions in the data in Figure 9 reflect pre-PETM conditions and that most of these proxies suggest decreasing oxygen concentrations across the PETM perturbation but without extensive anoxia leads to the conservative assumption that the pre-PETM ocean did not exhibit large-scale conditions too close to anoxia. In this regard, the simulated oxygen concentrations suggest that the ocean biogeochemical state in EE-noM2 is probably aberrant. This is confirmed by our calculation of the extent of anoxic seafloor, respectively 2.3% in EE-noM2 and 0.1% in EE-std, which also suggests an excess in oxygen depletion in EE-noM2 compared to pre-PETM estimates (Clarkson et al., 2021).

In addition, here, we do not *stricto sensu* model the biogeochemical conditions of the pre-PETM as, for instance, the global mean nutrient concentrations in phosphate, nitrate, alkalinity and silicate in the ocean are identical to the modern. Recent statistical box-modeling instead suggests that the marine phosphate concentrations reached a peak in the Paleogene, thus promoting higher primary productivity and lower deep-ocean O_2 concentrations (Sharoni & Halevy, 2023). All else being equal, prescribing a higher marine nutrient content in our simulations would decrease oxygen concentrations in both EE-noM2 and EE-std but with opposite effect on the model-data

comparison. In EE-std, this would reduce the model-data mismatch because simulated O₂ concentrations are likely too high whereas in EE-noM2, it would increase the proportion of anoxic waters and thereby increase the mismatch with estimates from the geological record. The model-data mismatch in EE-std could be even further reduced with a better representation of the smaller meridional temperature gradients that are inferred from proxy data (e.g., Evans et al., 2018; Huber & Caballero, 2011) because this would act to reduce the amount of oxygen stored in surface waters, and therefore decrease O₂ concentrations throughout the water column. This also implies that the simulated O₂ concentrations in EE-noM2 are likely a conservatively “high-concentration” estimate and thus that the aberrant biogeochemical state likely reflects an aberrant Early Eocene dynamical ocean in EE-noM2.

Finally, we note that the input energy dissipation from the M₂ tide that was used here is not exactly appropriate because the tidal model of Green and Huber (2013) was run with the ocean stratification obtained from the low-resolution equilibrated CCSM3 simulations discussed in Liu et al. (2009) instead of having been run with the IPSL-CM5A2 stratification. However, these simulations use a bathymetry close to that used in Green and Huber (2013) and the abyssal tidal dissipation is relatively insensitive to moderate changes in stratification. In addition, both our simulations and those of Liu et al. (2009) exhibit deep-water formation in the Southern Ocean. We thus argue that our results would not be significantly affected if the stratification from our simulations had been used in the tidal model simulations. In contrast, a larger impact is likely to be expected by the use of a higher-resolution bathymetric data set in an improved version of the tidal inversion model of Green and Huber (2013), such as that proposed in Green et al. (2023), and we aim to investigate this possibility in a near future. Alternatively, a promising way lies in the use of comprehensive tidal mixing schemes accounting for both near-field and far-field dissipation of internal tides (de Lavergne et al., 2020), rather than schemes fixing vertical diffusivity, such as the BL scheme, or including only near-field mixing, such as the S04 scheme used here.

5. Conclusion

Using Early Eocene IPSL-CM5A2 earth system model simulations, we demonstrate the critically overlooked impact of including a realistic estimate of the abyssal mixing driven by the near-field dissipation of internal tides in deep-time paleoclimate simulations. In our simulations, the global deep ocean circulation is substantially altered by the inclusion of abyssal tidal mixing, in particular in the Atlantic basin, and the global meridional overturning circulation is more intense and penetrates deeper in the ocean interior. This consequently drives large changes in the biogeochemical properties of deep water masses. In particular, we show that failing to include this abyssal turbulent mixing leads to a relatively stagnant deep North Atlantic ocean with large anoxic areas that compares less favorably to qualitative reconstruction of paleo-oxygenation for this period than the more energetic deep Atlantic ocean simulated in the experiment with realistic tidal mixing. Our results therefore stress the importance of routinely including abyssal turbulent mixing in upcoming deep-time paleoclimate studies and underline how the use of an adjunct biogeochemical model can help disentangle dynamical ocean modes for which proxies are lacking.

Conflict of Interest

The authors declare no conflicts of interest relevant to this study.

Data Availability Statement

Code availability. LMDZ, NEMO (including PISCES), ORCHIDEE, and XIOS are released under the terms of the CeCILL license. OASIS-MCT is released under the terms of the Lesser GNU General Public License (LGPL). IPSL-CM5A2 source code is available at http://forge.ipsl.fr/jgcmg/browser/CONFIG/publications/IPSLCM5A2_modipsl_rev6039_2023.

The model revision numbers used in this work can be found in the README file and are reported here:

- NEMOGCM branch nemo_v3_6_STABLE revision 6665
- XIOS2 branches/xios-2.5 revision 1903
- IOIPSL/src svn tags/v2_2_2
- LMDZ5 branches/IPSLCM5A2.1 rev 3907
- ORCHIDEE branches/ORCHIDEE-IPSLCM5A2.1 rev 7376

- OASIS3-MCT 2.0_branch (rev 4775 IPSL server)

We recommend to refer to the project website for a proper installation and compilation of the environment:

https://forge.ipsl.fr/igcmg_doc/wiki/Doc/Config/IPSLCM5A2, last accessed: 04/07/2024.

Model outputs. NetCDF outputs and scripts to produce the figures used in this study can be found in Ladant (2024).

Acknowledgments

We thank Matt Huber for editorial handling and two anonymous reviewers who helped improve the manuscript. We are grateful to Olivier Marti, Arnaud Caubel, Laurent Bopp, Olivier Aumont and Christian Ethé for discussions and help with the simulation setup. This work used computing hours on the HPC resources of the TGCC under GENCI allocations A0110102212 and A0130102212. NCL (<https://www.ncl.ucar.edu>) was used to make figures and most analyses, in addition to Fortran. Figures use color maps developed by Fabio Cramer (Cramer et al., 2020). JAMG acknowledges funding from the UK Natural Environment Research Council (Grants NE/F014821/1 and NE/S009566/1). YD acknowledges funding from the National Agency for Research (ANR) project OXYMORE (Grant 18-CE31-0020).

References

- Aumont, O., Ethé, C., Tagliabue, A., Bopp, L., & Gehlen, M. (2015). PISCES-v2: An ocean biogeochemical model for carbon and ecosystem studies. *Geoscientific Model Development*, 8, 2465–2513. <https://doi.org/10.5194/gmd-8-2465-2015>
- Blanke, B., & Delecluse, P. (1993). Variability of the tropical Atlantic Ocean simulated by a general circulation model with two different mixed-layer physics. *Journal of Physical Oceanography*, 23(7), 1363–1388. [https://doi.org/10.1175/1520-0485\(1993\)023<1363:VOTTAO>2.0.CO;2](https://doi.org/10.1175/1520-0485(1993)023<1363:VOTTAO>2.0.CO;2)
- Bopp, L., Resplandy, L., Untersee, A., Le Mezo, P., & Kageyama, M. (2017). Ocean (de) oxygenation from the Last Glacial Maximum to the twenty-first century: Insights from Earth system models. *Philosophical Transactions of the Royal Society A: Mathematical, Physical and Engineering Sciences*, 375(2102), 20160323. <https://doi.org/10.1098/rsta.2016.0323>
- Bryan, K., & Lewis, L. J. (1979). A water mass model of the World Ocean. *Journal of Geophysical Research*, 84(C5), 2503–2517. <https://doi.org/10.1029/JC084iC05p02503>
- Carmichael, M. J., Inglis, G. N., Badger, M. P. S., Naafs, B. D. A., Behrooz, L., Rimmelzwaal, S., et al. (2017). Hydrological and associated biogeochemical consequences of rapid global warming during the Paleocene-Eocene Thermal Maximum. *Global and Planetary Change*, 157, 114–138. <https://doi.org/10.1016/j.gloplacha.2017.07.014>
- Cimoli, L., Mashayek, A., Johnson, H. L., Marshall, D. P., Naveira Garabato, A. C., Whalen, C. B., et al. (2023). Significance of diapycnal mixing within the Atlantic meridional overturning circulation. *AGU Advances*, 4(2), e2022AV000800. <https://doi.org/10.1029/2022AV000800>
- Clarkson, M. O., Lenton, T. M., Andersen, M. B., Bagard, M.-L., Dickson, A. J., & Vance, D. (2021). Upper limits on the extent of seafloor anoxia during the PETM from uranium isotopes. *Nature Communications*, 12(1), 399. <https://doi.org/10.1038/s41467-020-20486-5>
- Cramer, F., Shephard, G. E., & Heron, P. J. (2020). The misuse of colour in science communication. *Nature Communications*, 11(1), 5444. <https://doi.org/10.1038/s41467-020-19160-7>
- de Lavergne, C., Groeskamp, S., Zika, J., & Johnson, H. L. (2022). The role of mixing in the large-scale ocean circulation. In *Ocean mixing* (pp. 35–63). Elsevier. <https://doi.org/10.1016/B978-0-12-821512-8.00010-4>
- de Lavergne, C., Madec, G., Roquet, F., Holmes, R. M., & McDougall, T. J. (2017). Abyssal ocean overturning shaped by seafloor distribution. *Nature*, 551(7679), 181–186. <https://doi.org/10.1038/nature24472>
- de Lavergne, C., Vic, C., Madec, G., Roquet, F., Waterhouse, A. F., Whalen, C. B., et al. (2020). A parameterization of local and remote tidal mixing. *Journal of Advances in Modeling Earth Systems*, 12(5), e2020MS002065. <https://doi.org/10.1029/2020MS002065>
- Dickson, A. J., Cohen, A. S., & Coe, A. L. (2012). Seawater oxygenation during the Paleocene-Eocene Thermal Maximum. *Geology*, 40(7), 639–642. <https://doi.org/10.1130/G32977.1>
- Dickson, A. J., Rees-Owen, R. L., März, C., Coe, A. L., Cohen, A. S., Pancost, R. D., et al. (2014). The spread of marine anoxia on the northern Tethys margin during the Paleocene-Eocene Thermal Maximum: Tethys redox during the PETM. *Paleoceanography*, 29(6), 471–488. <https://doi.org/10.1002/2014PA002629>
- Dunne, J. P., Sarmiento, J. L., & Gnanadesikan, A. (2007). A synthesis of global particle export from the surface ocean and cycling through the ocean interior and on the seafloor. *Global Biogeochemical Cycles*, 21(4), 2006GB002907. <https://doi.org/10.1029/2006GB002907>
- Egbert, G. D., & Ray, R. D. (2000). Significant dissipation of tidal energy in the deep ocean inferred from satellite altimeter data. *Nature*, 405(6788), 775–778. <https://doi.org/10.1038/35015531>
- Evans, D., Sago, N., Renema, W., Cotton, L. J., Müller, W., Todd, J. A., et al. (2018). Eocene greenhouse climate revealed by coupled clumped isotope-Mg/Ca thermometry. *Proceedings of the National Academy of Sciences of the United States of America*, 115(6), 1174–1179. <https://doi.org/10.1073/pnas.1714744115>
- Ferrari, R., & Ferreira, D. (2011). What processes drive the ocean heat transport? *Ocean Modelling*, 38(3–4), 171–186. <https://doi.org/10.1016/j.ocemod.2011.02.013>
- Fichefet, T., & Maqueda, M. A. M. (1997). Sensitivity of a global sea ice model to the treatment of ice thermodynamics and dynamics. *Journal of Geophysical Research*, 102(C6), 12609–12646. <https://doi.org/10.1029/97JC00480>
- Gargett, A. E. (1984). Vertical eddy diffusivity in the ocean interior. *Journal of Marine Research*, 42(2), 359–393. <https://doi.org/10.1357/002224084788502756>
- Garrett, C., & Kunze, E. (2007). Internal tide generation in the deep ocean. *Annual Review of Fluid Mechanics*, 39(1), 57–87. <https://doi.org/10.1146/annurev.fluid.39.050905.110227>
- Gaspar, P., Grégoris, Y., & Lefevre, J. (1990). A simple eddy kinetic energy model for simulations of the oceanic vertical mixing: Tests at station Papa and long-term upper ocean study site. *Journal of Geophysical Research*, 95(C9), 16179–16193. <https://doi.org/10.1029/JC095iC09p16179>
- Green, J. A. M., & Huber, M. (2013). Tidal dissipation in the early Eocene and implications for ocean mixing. *Geophysical Research Letters*, 40(11), 2707–2713. <https://doi.org/10.1002/grl.50510>
- Green, M., Hadley-Pryce, D., & Scotese, C. (2023). Phanerozoic (541 Ma-present day). In *A journey through tides* (pp. 157–184). Elsevier.
- Heinemann, M., Jungclauss, J. H., & Marotzke, J. (2009). Warm Paleocene/Eocene climate as simulated in ECHAM5/MPI-OM. *Climate of the Past*, 5(4), 785–802. <https://doi.org/10.5194/cp-5-785-2009>
- Heinz, M., & Ilyina, T. (2015). Ocean biogeochemistry in the warm climate of the late Paleocene. *Climate of the Past*, 11(1), 63–79. <https://doi.org/10.5194/cp-11-63-2015>
- Herold, N., Buzan, J., Seton, M., Goldner, A., Green, J. A. M., Müller, R. D., et al. (2014). A suite of early Eocene (~55 Ma) climate model boundary conditions. *Geoscientific Model Development*, 7(5), 2077–2090. <https://doi.org/10.5194/gmd-7-2077-2014>
- Holmes, R. M., Zika, J. D., Griffies, S. M., Hogg, A. M. C., Kiss, A. E., & England, M. H. (2021). The geography of numerical mixing in a suite of global ocean models. *Journal of Advances in Modeling Earth Systems*, 13(7), e2020MS002333. <https://doi.org/10.1029/2020MS002333>

- Hourdin, F., Foujols, M.-A., Codron, F., Guemas, V., Dufresne, J.-L., Bony, S., et al. (2013). Impact of the LMDZ atmospheric grid configuration on the climate and sensitivity of the IPSL-CM5A coupled model. *Climate Dynamics*, 40(9–10), 2167–2192. <https://doi.org/10.1007/s00382-012-1411-3>
- Huber, M., & Caballero, R. (2011). The early Eocene equable climate problem revisited. *Climate of the Past*, 7(2), 603–633. <https://doi.org/10.5194/cp-7-603-2011>
- Hutchinson, D. K., De Boer, A. M., Coxall, H. K., Caballero, R., Nilsson, J., & Baatsen, M. (2018). Climate sensitivity and meridional overturning circulation in the late Eocene using GFDL CM2.1. *Climate of the Past*, 14(6), 789–810. <https://doi.org/10.5194/cp-14-789-2018>
- Ilyina, T., & Heinze, M. (2019). Carbonate dissolution enhanced by ocean stagnation and respiration at the onset of the Paleocene-Eocene Thermal Maximum. *Geophysical Research Letters*, 46(2), 842–852. <https://doi.org/10.1029/2018GL080761>
- Jayne, S. R. (2009). The impact of abyssal mixing parameterizations in an ocean general circulation model. *Journal of Physical Oceanography*, 39(7), 1756–1775. <https://doi.org/10.1175/2009JPO4085.1>
- Krinner, G., Viovy, N., De Noblet-Ducoudré, N., Ogée, J., Polcher, J., Friedlingstein, P., et al. (2005). A dynamic global vegetation model for studies of the coupled atmosphere-biosphere system. *Global Biogeochemical Cycles*, 19(1), 2003GB002199. <https://doi.org/10.1029/2003GB002199>
- Ladant, J.-B. (2024). Model outputs and scripts to reproduce figures of a manuscript in revision in Paleoceanography & Paleoclimatology [Dataset]. *Zenodo*. <https://doi.org/10.5281/zenodo.10246070>
- Laugié, M., Donnadieu, Y., Ladant, J., Bopp, L., Ethé, C., & Raisson, F. (2021). Exploring the impact of Cenomanian paleogeography and marine gateways on oceanic oxygen. *Paleoceanography and Paleoclimatology*, 36(7), e2020PA004202. <https://doi.org/10.1029/2020PA004202>
- Lazar, A., Madec, G., & Delecluse, P. (1999). The deep interior downwelling, the Veronis effect, and mesoscale tracer transport parameterizations in an OGCM. *Journal of Physical Oceanography*, 29(11), 2945–2961. [https://doi.org/10.1175/1520-0485\(1999\)029<2945:TDIDTV>2.0.CO;2](https://doi.org/10.1175/1520-0485(1999)029<2945:TDIDTV>2.0.CO;2)
- Liu, Z., Pagani, M., Zinniker, D., DeConto, R., Huber, M., Brinkhuis, H., et al. (2009). Global cooling during the Eocene-Oligocene climate transition. *Science*, 323(5918), 1187–1190. <https://doi.org/10.1126/science.1166368>
- Lu, W., Rickaby, R. E. M., Hoogakker, B. A. A., Rathburn, A. E., Burkett, A. M., Dickson, A. J., et al. (2020). I/Ca in epifaunal benthic foraminifera: A semi-quantitative proxy for bottom water oxygen in a multi-proxy compilation for glacial ocean deoxygenation. *Earth and Planetary Science Letters*, 533, 116055. <https://doi.org/10.1016/j.epsl.2019.116055>
- Lunt, D. J., Bragg, F., Chan, W.-L., Hutchinson, D. K., Ladant, J.-B., Morozova, P., et al. (2021). DeepMIP: Model intercomparison of early Eocene climatic optimum (EECO) large-scale climate features and comparison with proxy data. *Climate of the Past*, 17(1), 203–227. <https://doi.org/10.5194/cp-17-203-2021>
- Lunt, D. J., Huber, M., Anagnostou, E., Baatsen, M. L. J., Caballero, R., DeConto, R., et al. (2017). The DeepMIP contribution to PMIP4: Experimental design for model simulations of the EECO, PETM, and pre-PETM (version 1.0). *Geoscientific Model Development*, 10(2), 889–901. <https://doi.org/10.5194/gmd-10-889-2017>
- MacKinnon, J. A., Zhao, Z., Whalen, C. B., Waterhouse, A. F., Trossman, D. S., Sun, O. M., et al. (2017). Climate process team on internal wave-driven ocean mixing. *Bulletin of the American Meteorological Society*, 98(11), 2429–2454. <https://doi.org/10.1175/BAMS-D-16-0030.1>
- Madec, G., Bourdallé-Badie, R., Boutier, P.-A., Bricaud, C., Bruciaferri, D., Calvert, D., et al. (2017). NEMO ocean engine. In *Notes du Pôle de modélisation de l'Institut Pierre-Simon Laplace (IPSL) (v3.6-patch, Numéro 27)*. Zenodo. <https://doi.org/10.5281/zenodo.3248739>
- Madec, G., & Imbard, M. (1996). A global ocean mesh to overcome the North Pole singularity. *Climate Dynamics*, 12(6), 381–388. <https://doi.org/10.1007/s003820050115>
- Marshall, J., & Speer, K. (2012). Closure of the meridional overturning circulation through Southern Ocean upwelling. *Nature Geoscience*, 5(3), 171–180. <https://doi.org/10.1038/ngeo1391>
- Meissner, K. J., Bralower, T. J., Alexander, K., Jones, T. D., Sijp, W., & Ward, M. (2014). The Paleocene-Eocene Thermal Maximum: How much carbon is enough? *Paleoceanography*, 29(10), 946–963. <https://doi.org/10.1002/2014PA002650>
- Melet, A., Legg, S., & Hallberg, R. (2016). Climatic impacts of parameterized local and remote tidal mixing. *Journal of Climate*, 29(10), 3473–3500. <https://doi.org/10.1175/JCLI-D-15-0153.1>
- Melet, A. V., Hallberg, R., & Marshall, D. P. (2022). The role of ocean mixing in the climate system. In *Ocean mixing* (pp. 5–34). Elsevier. <https://doi.org/10.1016/B978-0-12-821512-8.00009-8>
- Merryfield, W. J., Holloway, G., & Gargett, A. E. (1999). A global ocean model with double-diffusive mixing. *Journal of Physical Oceanography*, 29(6), 1124–1142. [https://doi.org/10.1175/1520-0485\(1999\)029<1124:AGOMWD>2.0.CO;2](https://doi.org/10.1175/1520-0485(1999)029<1124:AGOMWD>2.0.CO;2)
- Meurdesoif, Y., Caubel, A., Lacroix, R., Dérouillat, J., & Nguyen, M. H. (2016). *XIOS tutorial*. Retrieved from <http://forge.ipsl.jussieu.fr/ioserver/raw-attachment/wiki/WikiStart/XIOS-tutorial.pdf>
- Middelburg, J. J., Soetaert, K., Herman, P. M. J., & Heip, C. H. R. (1996). Denitrification in marine sediments: A model study. *Global Biogeochemical Cycles*, 10(4), 661–673. <https://doi.org/10.1029/96GB02562>
- Munk, W., & Wunsch, C. (1998). Abyssal recipes II: Energetics of tidal and wind mixing. *Deep-Sea Research*, 45(12), 1977–2010. [https://doi.org/10.1016/s0967-0637\(98\)00070-3](https://doi.org/10.1016/s0967-0637(98)00070-3)
- Munk, W. H. (1966). Abyssal recipes. *Deep-Sea Research*, 13(4), 707–730. [https://doi.org/10.1016/0011-7471\(66\)90602-4](https://doi.org/10.1016/0011-7471(66)90602-4)
- Pälike, C., Delaney, M. L., & Zachos, J. C. (2014). Deep-sea redox across the Paleocene-Eocene thermal maximum. *Geochemistry, Geophysics, Geosystems*, 15(4), 1038–1053. <https://doi.org/10.1002/2013GC005074>
- Saenko, O. A. (2006). The effect of localized mixing on the ocean circulation and time-dependent climate change. *Journal of Physical Oceanography*, 36(1), 140–160. <https://doi.org/10.1175/JPO2839.1>
- Saenko, O. A., & Merryfield, W. J. (2005). On the effect of topographically enhanced mixing on the global ocean circulation. *Journal of Physical Oceanography*, 35(5), 826–834. <https://doi.org/10.1175/JPO2722.1>
- Schmittner, A., & Egbert, G. D. (2014). An improved parameterization of tidal mixing for ocean models. *Geoscientific Model Development*, 7(1), 211–224. <https://doi.org/10.5194/gmd-7-211-2014>
- Schmittner, A., Green, J. A. M., & Wilmes, S.-B. (2015). Glacial ocean overturning intensified by tidal mixing in a global circulation model. *Geophysical Research Letters*, 42(10), 4014–4022. <https://doi.org/10.1002/2015GL063561>
- Sepulchre, P., Caubel, A., Ladant, J.-B., Bopp, L., Boucher, O., Braconnot, P., et al. (2020). IPSL-CM5A2—An Earth system model designed for multi-millennial climate simulations. *Geoscientific Model Development*, 13(7), 3011–3053. <https://doi.org/10.5194/gmd-13-3011-2020>
- Sharoni, S., & Halevy, I. (2023). Rates of seafloor and continental weathering govern Phanerozoic marine phosphate levels. *Nature Geoscience*, 16(1), 75–81. <https://doi.org/10.1038/s41561-022-01075-1>
- Simmons, H. L., Jayne, S. R., St. Laurent, L. C., & Weaver, A. J. (2004). Tidally driven mixing in a numerical model of the ocean general circulation. *Ocean Modelling*, 6(3–4), 245–263. [https://doi.org/10.1016/S1463-5003\(03\)00011-8](https://doi.org/10.1016/S1463-5003(03)00011-8)

- Song, P., Sidorenko, D., Scholz, P., Thomas, M., & Lohmann, G. (2023). The tidal effects in the Finite-volume Sea ice–Ocean Model (FESOM2.1): A comparison between parameterised tidal mixing and explicit tidal forcing. *Geoscientific Model Development*, *16*(1), 383–405. <https://doi.org/10.5194/gmd-16-383-2023>
- St. Laurent, L., & Garrett, C. (2002). The role of internal tides in mixing the deep ocean. *Journal of Physical Oceanography*, *32*(10), 2882–2899. [https://doi.org/10.1175/1520-0485\(2002\)032<2882:TROIIT>2.0.CO;2](https://doi.org/10.1175/1520-0485(2002)032<2882:TROIIT>2.0.CO;2)
- Talley, L. (2013). Closure of the global overturning circulation through the Indian, Pacific, and southern oceans: Schematics and transports. *Oceanography*, *26*(1), 80–97. <https://doi.org/10.5670/oceanog.2013.07>
- Thomas, D. J., Korty, R., Huber, M., Schubert, J. A., & Haines, B. (2014). Nd isotopic structure of the Pacific Ocean 70–30 Ma and numerical evidence for vigorous ocean circulation and ocean heat transport in a greenhouse world. *Paleoceanography*, *29*(5), 454–469. <https://doi.org/10.1002/2013PA002535>
- Toggweiler, J. R., & Samuels, B. (1995). Effect of Drake Passage on the global thermohaline circulation. *Deep-Sea Research Part A Oceanographic Research Papers*, *42*(4), 477–500. [https://doi.org/10.1016/0967-0637\(95\)00012-U](https://doi.org/10.1016/0967-0637(95)00012-U)
- Toggweiler, J. R., & Samuels, B. (1998). On the ocean's large-scale circulation near the limit of no vertical mixing. *Journal of Physical Oceanography*, *28*(9), 1832–1852. [https://doi.org/10.1175/1520-0485\(1998\)028<1832:OTOSLS>2.0.CO;2](https://doi.org/10.1175/1520-0485(1998)028<1832:OTOSLS>2.0.CO;2)
- Valcke, S. (2013). The OASIS3 coupler: A European climate modelling community software. *Geoscientific Model Development*, *6*(2), 373–388. <https://doi.org/10.5194/gmd-6-373-2013>
- Vic, C., Naveira Garabato, A. C., Green, J. A. M., Waterhouse, A. F., Zhao, Z., Melet, A., et al. (2019). Deep-ocean mixing driven by small-scale internal tides. *Nature Communications*, *10*(1), 2099. <https://doi.org/10.1038/s41467-019-10149-5>
- Wanninkhof, R. (1992). Relationship between wind speed and gas exchange over the ocean. *Journal of Geophysical Research*, *97*(C5), 7373–7382. <https://doi.org/10.1029/92JC00188>
- Weber, T., & Thomas, M. (2017). Influence of ocean tides on the general ocean circulation in the early Eocene. *Paleoceanography*, *32*(6), 553–570. <https://doi.org/10.1002/2016PA002997>
- Whalen, C. B., de Lavergne, C., Naveira Garabato, A. C., Klymak, J. M., MacKinnon, J. A., & Sheen, K. L. (2020). Internal wave-driven mixing: Governing processes and consequences for climate. *Nature Reviews Earth & Environment*, *1*(11), 606–621. <https://doi.org/10.1038/s43017-020-0097-z>
- Whitehead, J. A. (1998). Topographic control of oceanic flows in deep passages and straits. *Reviews of Geophysics*, *36*(3), 423–440. <https://doi.org/10.1029/98RG01014>
- Wilmes, S.-B., Green, J. A. M., & Schmittner, A. (2021). Enhanced vertical mixing in the glacial ocean inferred from sedimentary carbon isotopes. *Communications Earth & Environment*, *2*(1), 166. <https://doi.org/10.1038/s43247-021-00239-y>
- Winguth, A. M. E., Thomas, E., & Winguth, C. (2012). Global decline in ocean ventilation, oxygenation, and productivity during the Paleocene-Eocene Thermal Maximum: Implications for the benthic extinction. *Geology*, *40*(3), 263–266. <https://doi.org/10.1130/G32529.1>
- Xue, P., Chang, L., Dickens, G. R., & Thomas, E. (2022). A depth-transect of ocean deoxygenation during the Paleocene-Eocene Thermal Maximum: Magnetofossils in sediment cores from the southeast Atlantic. *Journal of Geophysical Research: Solid Earth*, *127*(8), e2022JB024714. <https://doi.org/10.1029/2022JB024714>
- Xue, P., Chang, L., & Thomas, E. (2023). Abrupt northwest Atlantic deep-sea oxygenation decline preceded the Palaeocene-Eocene Thermal Maximum. *Earth and Planetary Science Letters*, *618*, 118304. <https://doi.org/10.1016/j.epsl.2023.118304>
- Yao, W., Paytan, A., & Wortmann, U. G. (2018). Large-scale ocean deoxygenation during the Paleocene-Eocene Thermal Maximum. *Science*, *361*(6404), 804–806. <https://doi.org/10.1126/science.aar8658>
- Zhang, Y., De Boer, A. M., Lunt, D. J., Hutchinson, D. K., Ross, P., Van De Flierdt, T., et al. (2022). Early Eocene ocean meridional overturning circulation: The roles of atmospheric forcing and strait geometry. *Paleoceanography and Paleoclimatology*, *37*(3), e2021PA004329. <https://doi.org/10.1029/2021PA004329>
- Zhang, Y., Huck, T., Lique, C., Donnadieu, Y., Ladant, J.-B., Rabineau, M., & Aslanian, D. (2020). Early Eocene vigorous ocean overturning and its contribution to a warm Southern Ocean. *Climate of the Past*, *16*(4), 1263–1283. <https://doi.org/10.5194/cp-16-1263-2020>
- Zhou, X., Thomas, E., Rickaby, R. E. M., Winguth, A. M. E., & Lu, Z. (2014). ¹³C evidence for upper ocean deoxygenation during the PETM. *Paleoceanography*, *29*(10), 964–975. <https://doi.org/10.1002/2014PA002702>
- Zhou, X., Thomas, E., Winguth, A. M. E., Ridgwell, A., Scher, H., Hoogakker, B. A. A., et al. (2016). Expanded oxygen minimum zones during the late Paleocene-early Eocene: Hints from multiproxy comparison and ocean modeling. *Paleoceanography*, *31*(12), 1532–1546. <https://doi.org/10.1002/2016PA003020>